

## Time domain maximum likelihood parameter estimation in LISA Pathfinder data analysis

G. Congedo,<sup>\*</sup> L. Ferraioli,<sup>†</sup> M. Hueller, F. De Marchi, and S. Vitale*Dipartimento di Fisica, Università di Trento and INFN, Gruppo Collegato di Trento, 38123 Povo, Trento, Italy*

M. Armano

*European Space Agency (ESA), SRE-OD ESAC, 28692 Camino bajo del Castillo, Villanueva de la Cañada, Madrid*

M. Hewitson

*Albert-Einstein-Institut, Max-Planck-Institut für Gravitationsphysik und Universität Hannover, 30167 Hannover, Germany*

M. Nofrarias

*Institut de Ciències de l'Espai, (CSIC-IEEC), Facultat de Ciències, Campus UAB, Torre C-5, 08193 Bellaterra, Barcelona, Spain*

(Received 2 August 2011; published 18 June 2012)

LISA is the upcoming space-based gravitational-wave detector. LISA Pathfinder, to be launched in the coming years, will be the in-flight test of the LISA arm, with a hardware (control scheme, sensors, and actuators) identical in design to LISA. LISA Pathfinder will collect a picture of all noise disturbances possibly affecting LISA, achieving the unprecedented pureness of geodesic motion of test masses necessary for the detection of gravitational waves. The first steps of both missions will crucially depend on a very precise calibration of the key system parameters. Moreover, robust parameters estimation has a fundamental importance in the correct assessment of the residual acceleration noise between the test masses, an essential part of the data preprocessing for LISA. In this paper, we present a maximum likelihood parameter estimation technique in time domain employed for system identification, being devised for this calibration, and show its proficiency on simulated data and validation through Monte Carlo realizations of independent noise runs. We discuss its robustness to nonstandard scenarios possibly arising during the real mission. Furthermore, we apply the same technique to data produced in missionlike fashion during operational exercises with a realistic simulator provided by European Space Agency. The result of the investigation is that parameter estimation is mandatory to avoid systematic errors in the estimated differential acceleration noise.

DOI: [10.1103/PhysRevD.85.122004](https://doi.org/10.1103/PhysRevD.85.122004)

PACS numbers: 04.80.Nn, 02.60.Pn, 07.05.Kf

### I. INTRODUCTION

LISA [1,2] is the proposed space-based gravitational-wave (GW) detector planned to fly by the next decade. It is based on three spacecrafts (SCs)—each hosting and protecting two test masses (TMs) in nominal free fall—flying in a ( $5 \times 10^6$ ) km sided triangular formation around the Sun at 1 AU. A total of 6 TMs, whose displacements are detected by a laser-interferometric technique, constitute 6 Doppler links, two per LISA arm, tracking the local curvature variations around the Sun and being sensitive to the small fluctuations induced by GW signals in the 0.1–100 mHz band.

One (any) arm of LISA is virtually shrunk [3] to 38 cm and implemented in the LISA Pathfinder (LPF) mission [4,5]. LPF is the in-flight test of the LISA hardware, whose main goal is the measurement of the differential acceleration noise to within  $3 \times 10^{-14} \text{ m s}^{-2} \text{ Hz}^{-1/2}$  around

1 mHz—the minimum performance level for LISA to carry on its science program in astrophysics.

The observational horizon of LISA will include thousands of GW sources. Among all, the highest signal-to-noise sources will be surely the supermassive black holes. However, there are sources which are at the limit of the LISA sensitivity for which an accurate assessment of the instrumental noise is mandatory. The population of the extreme mass ratio inspirals (EMRIs) [6] is the most important example: they are a valuable instrument to test general relativity and curvature in the strong gravity regime. To date, different EMRI search methods have been developed. After having subtracted the highest signals (supermassive black holes and calibration binaries), in order to extract the EMRI signatures, all methods strictly have to deal with the instrumental noise level, for which the LPF mission has a crucial role. In fact, a systematic error in the reconstructed noise shape would dramatically affect the identification of such sources. The methods described in this paper allow for a solution of this problem.

The main payload onboard LPF, the LISA Technology Package (LTP) [7], will be used in an extensive characterization campaign by measuring all force disturbances and

<sup>\*</sup>congedo@science.unitn.it

<sup>†</sup>Present address: APC, Univ. Paris Diderot, CNRS/IN2P3, CEA/Ifnu, Obs de Paris, Sorbonne Paris Cité, France.

systematic errors. To the purpose, a precise calibration of the key system parameters must be performed before any assessment of the final level of differential acceleration noise can be made. The full process is iterative: the quality of free fall achieved at a given stage of the mission depends on the results of the previous experiments. By proceeding in the direction of increasing accuracy, the observed noise will be fully explained.

In LPF as a physical system, the relationship between the sensed relative motion and applied station-keeping forces plays a crucial role. Hence, the effect of the control forces must be taken into account and subtracted from the data, in order to provide a successful estimate of the residual acceleration noise. To this end, and to invert the system dynamics, the calibration of all key system parameters is required, a problem we address and solve by adopting a maximum likelihood parameter estimation in time domain. A preliminary work was presented in Ref. [8]; we hereby extend the method, present it in a more robust fashion, and apply it to simulated data sets, as well as to more realistic simulation data released by European Space Agency (ESA).

The paper is structured as follows. In Sec. II, we start by describing the LPF experiment with its main subsystems: sensors, controls, and actuators. In Sec. III, we introduce the sensed degrees of freedom, the control scheme, and the closed-loop equations of motion. Such an abstract formalism allows for a solution of the system inversion and the estimation of the acceleration noise out from the sensed relative motion. Then, we discuss a model along the two most relevant degrees of freedom—those sensing the relative motion of the TMs—which is used in our analysis and will be employed during the mission. Section IV gives a brief description of the most important contributions to the differential acceleration noise. In Sec. V, we describe the two experiments which are sufficient for the calibration of the system. As system identification has a capital importance to the correct assessment of the acceleration noise, we review the problem and solve it with a multi-input–multioutput (MIMO) multiexperiment approach. In turn, we describe the search algorithm and apply it to data produced by the ESA LPF science simulator; we validate the procedures by a Monte Carlo simulation; and finally, we proficiently apply the same techniques to a couple of non-standard scenarios: non-Gaussianities (glitches) in the readout and an underperforming system. The paper concludes with Sec. VII where we discuss the overall impact of system identification to the estimation of the residual acceleration noise: we demonstrate that without a preliminary identification of the modeled parameters, the reconstructed acceleration may be affected by systematic errors.

All analysis contained in this paper were performed under the framework of the LTP Data Analysis Toolbox [9], an objected-oriented extension of MATLAB [10] which will be extensively employed during the mission.

## II. LISA PATHFINDER EXPERIMENT

LTP—the main scientific payload onboard LPF—comprises the following key subsystems shown in Fig. 1: two gravitational reference sensors (GRSs), the optical metrology system (OMS) [interferometers (IFOs) and the optical bench], star trackers (STs), an onboard computer, the drag-free and attitude control system (DFACS), and the field emission electric propulsion (FEEP) thrusters. The experiment is also equipped with magnetometers, thermometers, and a cosmic charge counter. The sensors with the relative sensed motions are reported in Table I. The noise requirements are reported in Table II.

### A. Gravitational reference sensor

Each GRS comprises a gold-platinum cubic TM of size 46 mm and a surrounding electrostatic housing containing capacitive sensors and actuators in all 6 degrees of freedom. Each GRS senses the relative displacement and attitude of the TM to its housing and provides actuation along the same degrees of freedom. Gaps between the TM and its housing are 3–4 mm, a compromise between noise minimization and efficient sensing/actuation. The GRS vacuum chamber allows for a residual gas pressure at the level of 10  $\mu$ Pa. UV light illumination is utilized to control the accumulated charge with a discharging threshold of  $\sim 10^7$  e—the accumulated charge in 1 d for an expected charging rate of  $\sim 10^2$  e s $^{-1}$ . The sensing requirements of each GRS are 1.8 nm Hz $^{-1/2}$  in displacement and 200 nrad Hz $^{-1/2}$  in attitude. The actuation requirement is 20 fN Hz $^{-1/2}$  with a maximum range of 2.5 nN.

### B. Optical metrology system

The OMS [11] comprises: a Zerodur monolithic optical bench, 4 Mach-Zehnder heterodyne 1.024  $\mu$ m interferometers and redundant quadrant photodiodes. The first

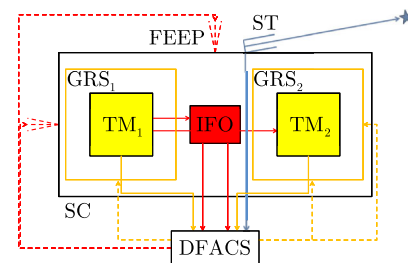


FIG. 1 (color online). Scheme of the key subsystems of the LPF mission. The SC contains two GRSs and an optical bench with four interferometers. The relative displacements and attitudes between the TMs and the optical bench are read out by the interferometers and the capacitive sensors. The interferometric, capacitive, and star-tracker readouts (solid lines) are fed into the DFACS which computes the forces which shall be actuated by the FEEP thrusters and the capacitive actuators (dashed lines). In the main science mode, the reference TM is not actuated along the optical axis.

TABLE I. LTP sensors and the relative sensed motions.

Sensor	Motion
GRS	linear and angular motion of the TMs relative to their housings
OMS	linear and angular motion of the reference TM relative to the optical bench linear and angular motion of the second TM relative to the reference TM
ST	absolute attitude of the SC

IFO,  $X_1$ , senses the relative displacement and attitude of one reference TM to the optical bench itself. The differential IFO,  $X_{12}$ , senses the relative displacement and attitude between the two TMs. Relative displacements are measured by averaging among the four quadrants, whereas relative angles are measured by taking the difference between opposite quadrants (differential wave-front sensing). The “reference” IFO is subtracted from the previous ones for compensating spurious fiber optical path length variations before the first beam splitter. The “frequency” IFO is utilized for laser frequency stabilization. The sensing requirements are  $9 \text{ pm Hz}^{-1/2}$  in displacement and  $20 \text{ nrad Hz}^{-1/2}$  in attitude with a maximum range of  $100 \text{ }\mu\text{m}$ . A rotation around the optical axis is not sensed, but can be provided by the GRS.

**C. Star trackers**

The STs are small telescopes reading out the inertial attitude of the SC with respect to the star field. The sensing requirement is  $32'' \text{ Hz}^{-1/2}$  ( $160 \text{ }\mu\text{rad Hz}^{-1/2}$ ).

**D. Drag-free and attitude control system**

The outputs of all sensors, GRSs, OMS, and STs are elaborated by the onboard computer and fed into the DFACS [12]. The DFACS has the responsibility of computing the control forces which shall be passed to capacitive and thruster actuators in order to stabilize the system and meet the acceleration requirement of  $3 \times 10^{-14} \text{ m s}^{-2} \text{ Hz}^{-1/2}$ .

There are different operational control modes for the LPF mission. To avoid large transients in the data, the transition between two modes is implemented with overlapping submodes. In the *accelerometer mode*, LPF acts as

a standard accelerometer in which the TMs are both electrostatically actuated along the optical axis and controlled to follow the SC motion. The resulting noise is much higher than the requirement. In the *main science mode*, the DFACS is responsible in maintaining a reference TM in free fall along the optical axis and forcing both the second TM and the SC to follow it by capacitive and thruster actuation.

The need for the DFACS is explained not only by the scientific requirements, but also by the fact that noise sources can destabilize the system on a time scale of few minutes, and the gaps between the TM and its housing are just 3–4 mm. One of the proposed activities, the free-flight experiment [13], is aimed at obtaining an improvement in differential acceleration noise at low frequency by turning off the capacitive actuation also on the second TM which is left in “parabolic” free fall and impulsively kicked every 200 s.

In the main science mode, the DFACS is conceptually divided into three control loops with the following priority:

- (1) *drag-free control loop*, controlling the relative displacement and attitude of the SC with respect to the reference TM through thruster actuation;
- (2) *electrostatic suspension control loop*, controlling the relative displacement and attitude between the TMs through capacitive actuation on the second TM;
- (3) *attitude control loop*, controlling the inertial (absolute) attitude of the TMs through capacitive actuation.

The drag-free requirements are  $5\text{--}6 \text{ nm Hz}^{1/2}$  in displacement and  $0.4\text{--}0.5 \text{ }\mu\text{rad Hz}^{1/2}$  in attitude.

TABLE II. LTP key subsystems and the main noise requirements around 1 mHz.

Subsystem	Requirement	Note
GRS	$1.8 \text{ nm Hz}^{-1/2}$ $20 \text{ fN Hz}^{-1/2}$	displacement sensing actuation
OMS	$9 \text{ pm Hz}^{-1/2}$ $20 \text{ nrad Hz}^{-1/2}$	displacement sensing attitude sensing
ST	$32'' \text{ Hz}^{-1/2}$	...
DFACS	$5\text{--}6 \text{ nm Hz}^{1/2}$ $0.4\text{--}0.5 \text{ }\mu\text{rad Hz}^{1/2}$	displacement control (main science mode) attitude control (main science mode)
FEEP	$0.1 \text{ }\mu\text{N Hz}^{-1/2}$	...

### E. Thrusters

The FEED is attained by an ensemble of 3 clusters, of 4 thrusters each, attached to the SC. An electron flux keeps the SC neutral. The force requirement is  $0.1 \mu\text{NHz}^{-1/2}$  with a maximum range of  $100 \mu\text{N}$ . The FEED thruster authority is the only means by which the reference TM can be maintained in free fall along the optical axis, hence mitigating the SC jitter at low frequency. The SC is also equipped with colloid thrusters provided by NASA for complementary experiments.

Recently, ESA has considered the possibility to employ cold gas thrusters in place of the FEED. The new design is expected to perform to within the requirements as well. However, the considerations and the results of this paper are still valid and are not appreciably affected by the possible change in design.

## III. DYNAMICS

The formalism developed in this section is effective in mapping a complex dynamics into a simple equation, treating different aspects of the system at the same time as a whole, and allowing for the reconstruction of the total input differential acceleration from the interferometrically sensed motion.

Like every physical dynamical system, LPF can be described by three main conceptual parts:

- (1) free dynamics;
- (2) sensing;
- (3) control and actuation.

The first one is the natural free evolution of the system. This gives the dynamical evolution of the TMs as they were left alone in their flight. However, small unwanted disturbances can take each TM away from the ideal geodesic, the *reference* trajectory. On-ground measurements and models predict that to first order the TMs are electrostatically coupled with the SC through negative force gradients described by unstable oscillators. If the TMs were left to follow their free evolution, the system would exponentially destabilize in a very small timescale. Referring to Fig. 1, in the main science mode, the sensed motion between the TM and the interferometer and the sensed relative motion between the TMs is fed into the DFACS controller to command actuation on the SC and the second TM to both follow the reference TM. In this way, one would say that the controller utilizes the sensed relative motion to suppress the disturbances by “pushing” a body toward the reference trajectory, i.e., by actuating it along specific degrees of freedom.

In turn, Sec. III A lists the relevant coordinates in LPF, the sensors, the control laws, and the actuators for each degree of freedom; Sec. III B provides for a general description of the adopted control scheme; Sec. III C introduces the generalized equation of motion for LPF; finally, Sec. III D describes the model along the optical axis employed for the analysis of this paper.

### A. Coordinate definitions

LPF is a 3-body dynamical system composed by a SC containing two TMs, whose relative motion is sensed by an interferometer and the capacitive sensors, as described in the preceding section. As LPF characterizes the relative motion between those bodies, the inertial acceleration of the SC is not sensed. Therefore, the degrees of freedom of the system are:

- (1) the relative translations of the TM with respect to the SC,  $3 + 3$ ;
- (2) the relative attitudes of the TM with respect to the SC,  $3 + 3$ ;
- (3) additionally, the absolute (inertial) attitude of the SC with respect to the celestial frame, 3.

The naming convention for the sensed coordinates in LPF in science mode can be found in Fig. 2. There are 15 control laws implemented by the DFACS, 12 for the TM relative motions, and 3 for the SC absolute attitude. A coordinate guiding the drag-free loop, i.e., a thruster actuation on the SC, is named *drag-free coordinate*. Analogously, a coordinate guiding the electrostatic suspension loop, i.e., a capacitive actuation on the TMs, is named *electrostatic suspension coordinate*. Finally, a coordinate guiding the attitude loop, i.e., a capacitive actuation on the TMs to maintain the inertial orientation, is named *attitude coordinate*. The names of the control loops, the sensor readouts used as inputs to the control laws, and the actuators are reported in Table III for all controlled degrees of freedom in the main science mode.

Basically, in the main science mode, all optical readings are used whenever possible and:

- (1) along  $x$ : guided by the optical  $x_1$ , the SC is forced to follow the reference TM through thruster actuation; guided by the optical  $x_{12}$ , the second TM is forced to follow the reference TM through capacitive actuation;
- (2) along orthogonal degrees of freedom: guided by the average linear motion of the TMs read out by the capacitive sensors, the SC is forced to follow both

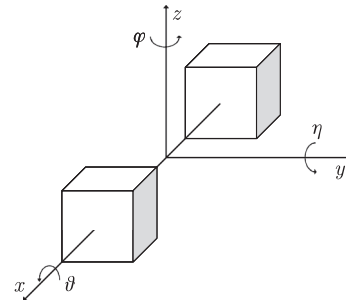


FIG. 2. Coordinate naming convention for the 3-body LPF system. The  $x$  axis is the laser sensitive translational degree of freedom, and the  $\eta$  and  $\phi$  angles are optically detected. The  $\theta$  angle is not interferometrically detectable. Other coordinates can be read out by capacitive sensors, especially along  $y$  and  $z$ .

TABLE III. List of all controlled degrees of freedom for the LPF mission in the main science mode. The drag-free, electrostatic suspension, and attitude control loops, together with the interferometer, capacitive, and star-tracker sensors and the thruster and capacitive actuators are reported for each coordinate. Interferometric sensing is used in place of the capacitive whenever possible. Notice that the interferometer measures the relative linear and angular motion between the TMs, i.e.,  $x_{12} = x_2 - x_1$ ,  $\eta_{12} = \eta_2 - \eta_1$ , and  $\phi_{12} = \phi_2 - \phi_1$ . The SC absolute position is not sensed.

Coordinate	Control	Sensor	Actuator
$x_1$	Drag-free	$o_1 = \text{IFO}[x_1]$	FEEP
$y_1$	Drag-free	$o_{y_1} = \text{GRS}[y_1]$	FEEP
$z_1$	Drag-free	$o_{z_1} = \text{GRS}[z_1]$	FEEP
$\theta_1$	Drag-free	$o_{\theta_1} = \text{GRS}[\theta_1]$	FEEP
$\eta_1$	Electrostatic suspension	$o_{\eta_1} = \text{IFO}[\eta_1]$	GRS
$\phi_1$	Electrostatic suspension	$o_{\phi_1} = \text{IFO}[\phi_1]$	GRS
$x_2$	Electrostatic suspension	$o_{12} = \text{IFO}[x_{12}]$	GRS
$y_2$	Drag-free	$o_{y_2} = \text{GRS}[y_2]$	FEEP
$z_2$	Drag-free	$o_{z_2} = \text{GRS}[z_2]$	FEEP
$\theta_2$	Electrostatic suspension	$o_{\theta_2} = \text{GRS}[\theta_2]$	GRS
$\eta_2$	Electrostatic suspension	$o_{\eta_{12}} = \text{IFO}[\eta_{12}]$	GRS
$\phi_2$	Electrostatic suspension	$o_{\phi_{12}} = \text{IFO}[\phi_{12}]$	GRS
$\theta_{\text{SC}}$	Attitude	$o_{\theta_{\text{SC}}} = \text{ST}[\theta_{\text{SC}}]$	GRS
$\eta_{\text{SC}}$	Attitude	$o_{\eta_{\text{SC}}} = \text{ST}[\eta_{\text{SC}}]$	GRS
$\phi_{\text{SC}}$	Attitude	$o_{\phi_{\text{SC}}} = \text{ST}[\phi_{\text{SC}}]$	GRS

TMs through thruster actuation; guided by the star-tracker inertial attitude, the TMs are oriented through capacitive actuation;

- (3) along rotational degrees of freedom: guided by the differential linear motion of the TMs read out by the capacitive sensors, the SC is forced to follow both TMs through thruster actuation; guided by the optical TM attitudes, both TMs are oriented through capacitive actuation.

**B. Controller**

The controller is a dynamical system (see Fig. 3), in general multidimensional, taking the difference between the measured and the reference trajectories as inputs and producing forces to be applied to the bodies as outputs. If  $\mathbf{o}$  is the sensed motion, the *error* signals for all controlled degrees of freedom are

$$\mathbf{e} = \mathbf{o} - \mathbf{o}_i, \tag{1}$$

where  $\mathbf{o}_i$  are named *reference set-point* signals or simply *guidance* signals.

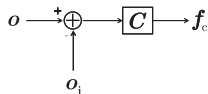


FIG. 3. Block diagram of the controller. It takes the differences between the measured coordinates  $\mathbf{o}$  and the reference coordinates  $\mathbf{o}_i$  and calculates control forces  $\mathbf{f}_c$  to be applied to the SC and the TMs.

The DFACS is responsible of the minimization of the error signals. In this way, it compensates for negative force gradients and makes the system stable. It utilizes the sensed relative motion along different degrees of freedom, contained in the error signal, to compute actuation forces  $\mathbf{f}_c$ . The discrete implementation of the  $n$ th value of the commanded force  $f_{c,n}$ , for a generic control law in LPF controlling a single degree of freedom, is a linear combination of the past values of the force  $f_{c,n-1}, f_{c,n-2}, \dots$  and the present and past values of the error signal (the innovations)  $e_n, e_{n-1}, \dots$

$$f_{c,n} = \sum_i q_i f_{c,n-i} + \sum_j p_j e_{n-j}, \tag{2}$$

where  $i = 1, \dots, N_q$  and  $N_q$  is the order of the autoregressive filter;  $j = 0, \dots, N_p$ ; and  $N_p$  is the order of the moving average filter. The  $z$ -transform of the above gives the well-known autoregressive moving average model of the discrete control law:

$$C(z) = \frac{\sum_j p_j z^{-j}}{1 - \sum_i q_i z^{-i}}. \tag{3}$$

The control design assures: (i) the compensation of negative force gradients; (ii) the asymptotic stability; (iii) the mitigation of system resonances; and (iv) the minimal-cost performance, i.e., the control computes the minimum actuation forces which allow the TMs to reach the reference signals to within the given accuracy of

5 nm Hz<sup>-1/2</sup> around 1 mHz (for the relative displacement control as reported in Table II), whose unsuppressed part contributes to the residual noise budget. ASTRIUM [14]—the main industry contractor of LPF—has provided the continuous representation of the controller as a rational function in the  $s$  domain (of maximum order 6), used for system modeling, simulation, and analysis shown in this paper.

### C. Equation of motion

This section describes the formalism on the basis of the modeling of the closed-loop LPF system. The most important assumption concerns on the linearity of the equations, i.e., that all physical quantities characterizing the motion enter linearly into the equations. Here is a list of the involved limitations:

- (1) the force couplings between the TMs and the SC are mainly caused by electrostatics and SC self-gravity: those forces decay as the inverse of the distance at most; they are treated to first order as springlike forces;
- (2) the interferometric sensing involves reflections and transmissions through optical elements: even in geometric optics, the equations must involve trigonometric expressions of the angles; it is assumed that trigonometric functions confuse with angles, whenever applicable;
- (3) the angular motion of a rigid body is described by the Euler equations: they are nonlinear with respect to the angular velocities; if the angular motion is small, nonlinearities are a second-order effect.

Since the controller forces the motion around the reference trajectories, it also assures that the motion is small enough that all forces and nonlinear terms can be expanded to first order with good approximation. In this way, the coupling forces are modeled as negative springlike constants; the nonlinearities due to optics and the angular motion can be effectively ignored. In general, the linearized equations of motion must contain terms to within the order of an imperfection multiplied by a noise contribution. In fact, other combinations like a noise contribution multiplied by another noise contribution are second-order effects and must be neglected. The accuracy to which linearity is achieved depends on: (i) the assumption that the controller does not itself introduce nonlinearities in the system; and (ii) the unsuppressed noisy motion in the error signals is to within the requirement figure of the controller.

We now focus our attention on a model for LPF elaborated in terms of the two main degrees of freedom, i.e.,

$$s^2 x_1 + s^2 x_{SC} + \omega_1^2 x_1 + \Gamma_x (x_2 - x_1) = f_1, \quad (4a)$$

$$s^2 x_2 + s^2 x_{SC} + \omega_2^2 x_2 - \Gamma_x (x_2 - x_1) = f_2 - C_{sus}(s) o_{12}, \quad (4b)$$

$$s^2 x_{SC} - \tilde{m}_1 \omega_1^2 x_1 - \tilde{m}_2 \omega_2^2 x_2 = f_{SC} + C_{df}(s) o_1 - \tilde{m}_1 f_1 - \tilde{m}_2 f_2 + \tilde{m}_2 C_{sus}(s) o_{12}, \quad (4c)$$

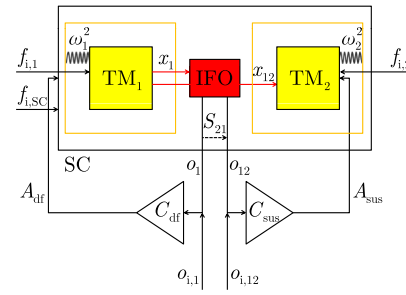


FIG. 4 (color online). Scheme of the LPF model along the optical axis in the main science mode. The first TM is in free fall along  $x$ , and its displacement to the optical bench ( $o_1$ ) is sensed by the IFO and fed into the controller ( $C_{df}$ ) to force the SC to follow the TM through thruster actuation (drag-free loop). Analogously, the sensed differential displacement between the two TMs ( $o_{12}$ ) is fed into the controller ( $C_{sus}$ ) to force the TM to follow the reference one through capacitive actuation (suspension loop). The critical system parameters are the TM springlike couplings to the SC ( $\omega_1^2$  and  $\omega_2^2$ ), the sensing cross-talk ( $S_{21}$ ), and the actuation gains ( $A_{df}$  and  $A_{sus}$ ). The system can be excited by injecting signals as direct forces on the masses ( $f_{i,1}$ ,  $f_{i,2}$ , and  $f_{i,SC}$ ) or controller guidance signals ( $o_{i,1}$  and  $o_{i,12}$ ).

those along the optically sensed axis: the relative motion of the reference TM to the optical bench and the differential motion between the TMs. In this formulation, the relative motion is sensed with the interferometer—the reference measurement for scientific operations—while keeping in mind that the capacitive sensors could even be used in place of the interferometer as a backup option, even though such a measurement would be 2 orders of magnitude worse, especially at high frequency. However, along the other orthogonal axes, the capacitive sensors are the only means by which the TM relative motion can be measured. Figure 4 shows a sketch of a LPF model, in the main science mode, along the optical axis being discussed here in details.

Referring to Figs. 2 and 4,  $x$  is the interferometric axis.  $x_{SC}$  is the absolute SC position, and  $x_1$ ,  $x_2$  are the relative TM positions with respect to the SC;  $m_{SC} = 422.7$  kg and  $m_1 = m_2 = 1.96$  kg are the respective masses;  $\tilde{m}_1 = \tilde{m}_2 = 5 \times 10^{-3}$  are the masses normalized to  $m_{SC}$ ; and  $f_1$ ,  $f_2$ , and  $f_{SC}$  are the total forces (per unit mass) containing noise in any form and applied biases.

In the linear approximation (small motion, small forces, as already discussed), the 3-body dynamics is described by a linear system of differential equations. In frequency domain and assuming null initial conditions, the equations of motion are

where  $\omega_1^2 \approx \omega_2^2 \sim -1 \times 10^{-6} \text{ s}^{-2}$  are spring constants modeling oscillatorlike force couplings between the TMs and the SC, named *parasitic stiffness*. As the dominating part of such force gradients is due to electrostatics, the oscillators are unstable: that is the reason why a controller is employed.  $\Gamma_x \sim 4 \times 10^{-9} \text{ s}^{-2}$  is the gravity gradient (per unit mass) between the TMs corresponding to a nominal separation of  $\sim 38 \text{ cm}$ . All terms containing normalized masses are backreactions which can be neglected to zeroth order.

In writing the dynamics, the control in the science mode is implicitly assumed, where the SC is forced to follow a reference TM in free fall along the optical axis, and the other TM is forced to follow the reference TM along the same axis. As declared by Table III, the interferometric readout  $o_1$  ( $x_1$  coordinate) is a drag-free coordinate and is the input to the drag-free control law  $C_{\text{df}}(s)$  assuring thruster actuation. The interferometric readout  $o_{12}$  ( $x_{12} = x_2 - x_1$  coordinate) is an electrostatic suspension coordinate and is the input to the electrostatic suspension control law  $C_{\text{sus}}(s)$  assuring capacitive actuation on the second TM.

With these assumptions, LPF is viewed as a closed-loop MIMO linear time-invariant dynamical system described by vector equations with operators modeling dynamics, sensing, and control. The linearized equations for LPF are [15–17]

$$Dq = g, \quad (5a)$$

$$g = f_n + A[f_i - C(o - o_i)], \quad (5b)$$

$$o = Sq + o_n. \quad (5c)$$

The total forces (per unit mass)  $g$  produce the motion through the acting of the dynamics operator  $D$  onto the physical coordinates  $q$ . The natural physical coordinates for LPF are given by the TM relative linear and angular motion.  $D$  is a differential operator containing time derivatives and the modeled coupling coefficients (the negative spring constants due to the linearization) and the dynamical cross-talk from other degrees of freedom to the sensitive axis as well. In fact, the dynamics along the measurement axis (the nominal dynamics) can be decoupled from the dynamics along other degrees of freedom (the first-order perturbation) employing a generalization of the above formalism. The external forces can be split into pure noise sources  $f_n$ —mostly from the SC jitter and within the TM housings; applied biases  $f_i$ —directly on each TM and the SC; and applied biases through  $o_i$ —the controller guidance signals already discussed in the preceding subsection.  $C$  is the operator containing the control laws. By changing the controller guidance signals, net forces on each body are commanded to the actuators

$$f_c = -C(o - o_i), \quad (6)$$

where  $o$  is the closed-loop measurement. Therefore, the application of biases in the controller guidance signals is equivalent to the application of explicit forces on the

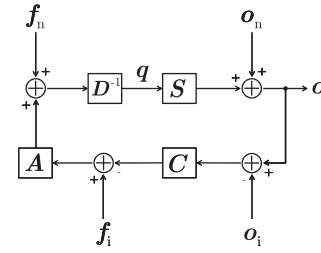


FIG. 5. Block diagram for the three main conceptual steps of LPF: dynamics, sensing, and control. There are two different noise sources,  $f_n$  and  $o_n$ , and biases to inject,  $f_i$  and  $o_i$ . The open loops are defined by the transfers from forces to readouts. The forces produce the motion in the  $q$  coordinates through the inverse of  $D$ . The coordinates are converted into sensed coordinates  $o$  through  $S$ . The controller closes the loop in order to minimize the error signals, through  $C$  applied to the sensed coordinates. The calculated forces are then converted into actuation forces through  $A$ .

bodies. In this description, the application of the forces is modeled by an actuation operator  $A$ . All force biases and control forces are fed into such an operator, responsible of the force dispatching on all bodies. In the main science mode, along the measurement axis, this implies a thruster actuation on the SC to follow the reference TM in free fall and a capacitive actuation on the second TM to follow the reference TM. Finally, the physical coordinates  $q$  are converted into the system readouts  $o$  (from interferometric and capacitive sensors) through the sensing operator  $S$ , mostly diagonal, and corrupted by the readout noise  $o_n$ .  $S$  is nominally an identity operator, but in reality, there is a sensing cross-talk between different readout channels and miscalibrations as well. Figure 5 shows the block diagram of the closed-loop dynamics for LPF where all operators act on their own inputs and produce their outputs for the dynamical equations in Eqs. (5); deterministic and stochastic inputs are also distinguished for clarity.

The full equation of motion in vector form and expressed in terms of the sensed relative coordinates,  $o$ , can be obtained by manipulating the three equations in Eqs. (5). The idea is to substitute Eq. (5c) and Eq. (5b) in Eq. (5a) and rearrange the equation so that the deterministic and stochastic inputs are on the right-hand side. The result is the *equation of motion in the sensed coordinates*

$$\Delta o = f_n + DS^{-1}o_n + A(f_i + Co_i), \quad (7)$$

where four terms are clearly recognized: force noise, readout noise, force bias, and controller guidance bias, which all constitute the noise budget of LPF in terms of total equivalent acceleration. The second-order differential operator on the right-hand side is defined as

$$\Delta = DS^{-1} + AC. \quad (8)$$

The deep meaning of the operator is that it allows for the reconstruction of the total equivalent input acceleration

from the sensed relative motion and at the same time isolating and subtracting dynamics, sensing, control, and actuation. Indeed, by looking at Fig. 5,  $\mathbf{DS}^{-1}$  is the *open loop* from the sensed relative motion to input forces (inverting the direction of an arrow, the corresponding operator must be inverted); whereas  $\mathbf{AC}$  is the *control loop* consisting of all control laws commanding the force actuation.

In Eq. (7), two transfer operators can be naturally identified

$$\mathbf{T}_{o \rightarrow f} = \mathbf{\Delta}, \quad (9a)$$

$$\mathbf{T}_{o_i \rightarrow o} = \mathbf{\Delta}^{-1} \mathbf{AC}. \quad (9b)$$

The second one solves the equation of motion for deterministic guidance signals and, substituted into Eq. (6), gives the following transfer operator:

$$\mathbf{T}_{o_i \rightarrow f_c} = -\mathbf{C}(\mathbf{T}_{o_i \rightarrow o} - 1), \quad (10)$$

converting the bias injections  $o_i$  into the calculated control forces which the actuators must apply in order to stabilize the motion toward the reference signal.

The first transfer operator  $\mathbf{T}_{o \rightarrow f}$  has fundamental relevance as it shows that the differential operator allows for the *estimation of the total out-of-loop equivalent acceleration noise* [18] on noisy interferometric data, i.e., when all explicit stimuli are set to zero, whose modeling in terms of force noise and readout noise is provided by the equation of motion (7). However, the evaluation requires the calibration of the dynamics  $\mathbf{D}$ , the sensing  $\mathbf{S}$ , and the actuation  $\mathbf{A}$  operators overall depending on many system parameters. This critical procedure, named *system identification*, which

the performances of the LPF mission depend on, will be outlined in Sec. VI. It mainly consists of calibrating the second transfer operator  $\mathbf{T}_{o_i \rightarrow o}$  and estimating all system parameters in dedicated experiments.

#### D. Dynamical model along the optical axis

In order to get to a dynamical model in the form of equations like Eqs. (5) which can be used for the analysis, the first step is to rearrange Eqs. (4) to eliminate the unmeasurable absolute position  $x_{\text{SC}}$  and rewrite the equations in terms of the 2 degrees of freedom  $x_1$  and  $x_{12}$ . In fact, by taking the difference between Eqs. (4b) and (4a), the SC acceleration vanishes. Then, the SC acceleration in Eq. (4c) is substituted in Eq. (4a). The structure of the equations suggests to define the *differential forces*  $f_{12} = f_2 - f_1$  and the *differential parasitic stiffness*  $\omega_{12}^2 = \omega_2^2 - \omega_1^2$ . The equations can be finally condensed into the formalism of Eq. (5a), where the dynamics operator has the following matrix representation:

$$\mathbf{D} = \begin{pmatrix} s^2 + (1 + \tilde{m}_1 + \tilde{m}_2)\omega_1^2 + \tilde{m}_2\omega_{12}^2 & \Gamma_x + \tilde{m}_2(\omega_1^2 + \omega_{12}^2) \\ \omega_{12}^2 & s^2 + \omega_1^2 + \omega_{12}^2 - 2\Gamma_x \end{pmatrix}, \quad (11)$$

which, acting on the system coordinates

$$\mathbf{q} = \begin{pmatrix} x_1 \\ x_{12} \end{pmatrix}, \quad (12)$$

produces the external forces

$$\mathbf{g} = \begin{pmatrix} (1 + \tilde{m}_1 + \tilde{m}_2)f_1 + \tilde{m}_2f_{12} - f_{\text{SC}} - C_{\text{df}}(s)o_1 - \tilde{m}_2C_{\text{sus}}(s)o_{12} \\ f_{12} - C_{\text{sus}}(s)o_{12} \end{pmatrix}. \quad (13)$$

The preceding contains force noise sources and injected biases. Neglecting all backreactions, it shows that the first degree of freedom  $x_1$  is dominated by the thruster noise and the drag-free actuation; the second degree of freedom  $x_{12}$  is dominated by the differential force noise and the capacitive actuation on the second TM. The identified control operator of Eq. (5b) is given by

$$\mathbf{C} = \begin{pmatrix} C_{\text{df}}(s) & \tilde{m}_2C_{\text{sus}}(s) \\ 0 & C_{\text{sus}}(s) \end{pmatrix}, \quad (14)$$

where the off-diagonal quantity is the backreaction from the suspension to the drag-free loop.

The dynamical equations shown above assume a perfect actuation. This implies that  $\mathbf{A}$  is an identity. Otherwise, actuation gains  $A_{\text{df}}$ , and  $A_{\text{sus}}$  may be conveniently introduced to model the efficiency to which commanded forces are converted to actual applied forces by the corresponding loops.

The expression in Eq. (5c) gives the sensing conversion between the physical coordinates  $\mathbf{q}$  and the interferometric readouts,

$$\mathbf{o} = \begin{pmatrix} o_1 \\ o_{12} \end{pmatrix}, \quad (15)$$

being fed up into the controller. The perfect conversion is represented by an identity matrix. The imperfect conversion is due to both miscalibrations (the diagonal terms) or cross-talk contributions (the off-diagonal terms). The on-ground characterization and the theoretical modeling of the interferometer [19] suggest that the most relevant is the cross-talk from  $o_1$  to  $o_{12}$  which mixes the two nominally independent degrees of freedom in the following way:

$$\mathbf{S} = \begin{pmatrix} 1 & 0 \\ S_{21} & 1 \end{pmatrix}. \quad (16)$$

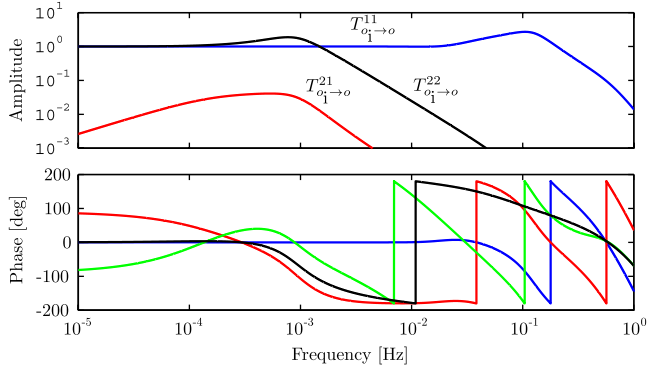


FIG. 6 (color online). Frequency dependence of the transfer matrix  $T_{o_i \to o}$  used for system identification. The transfer function  $T_{o_i \to o}^{11} = T_{o_{i,1} \to o_{i,1}}$  has peak gain of almost 3 at 0.1 Hz. The transfer function  $T_{o_i \to o}^{22} = T_{o_{i,12} \to o_{i,12}}$  has peak gain of about 2 at 0.8 mHz, then it quickly decays. The dynamical cross-talk  $T_{o_i \to o}^{12} = T_{o_{i,1} \to o_{i,12}}$  has peak gain of about  $5 \times 10^{-2}$  at 0.5 mHz. The other dynamical cross-talk is negligible since it has peak gain of about  $4 \times 10^{-6}$  at 30 mHz.

The cross-talk is explained by a tiny difference in the incidence angles with which light reflects on the TM surface for the two readings.

As described in Sec. III D, the system can be modeled by the operators  $D$  (dynamics),  $S$  (sensing), and  $A$  (actuation) representing different nonidealities in the practical implementation of the closed-loop LISA arm. The operators contain all system parameters describing the dynamics along the optical axis. One last source of indetermination introduced here is a delay in the application of the guidance signals

$$\mathbf{T} = \begin{pmatrix} e^{-s\Delta t_1} & 0 \\ 0 & e^{-s\Delta t_2} \end{pmatrix}, \quad (17)$$

whose possible causes may be either due to the digitalization of the continuous control laws or to bus delays, a possibility

not considered in a previous model [20]. With the introduction of the delays, the model (9b) becomes now

$$\mathbf{T}_{o_i \to o} = \mathbf{\Delta}^{-1} \mathbf{A} \mathbf{C} \mathbf{T}, \quad (18)$$

where the differential operator  $\mathbf{\Delta}$ , defined in Eq. (9a), converts the sensed motion into total equivalent acceleration.

Figure 6 shows the transfer gains of the model  $T_{o_i \to o}$ , whereas the dynamical cross-talk from the differential channel to the first one is definitely negligible with a peak gain of about  $4 \times 10^{-6}$  at 30 mHz. The diagonal elements have, respectively, peak gains of almost 3 at 0.1 Hz and about 2 at 0.8 mHz. The dynamical cross-talk from the first channel to the differential one has peak gain of about  $5 \times 10^{-2}$  at 0.5 mHz. The above transfer matrix is used to both model the outputs of the system subjected to bias injections and perform system identification.

Throughout this paper, bias injections at the level of controller guidance signals  $\mathbf{o}_i$  [21] are considered, and the transfer matrix in Eq. (18) models the response of the system to those signals. As the modeled system parameters appear in the operators,  $T_{o_i \to o}$  is parameter-dependent. The modeled system response is then parameter-dependent. The parameters can be arranged in a vector which will be abstractly referred to  $\mathbf{p}$

$$\mathbf{p} = \begin{pmatrix} \omega_1^2 \\ \omega_{12}^2 \\ S_{21} \\ A_{df} \\ A_{sus} \\ \Delta t_1 \\ \Delta t_2 \end{pmatrix}, \quad (19)$$

where Table IV provides a description of the above system parameter with initial plausible estimates coming from on-ground measurements and theoretical modeling.

TABLE IV. List of the modeled system parameters, introduced in Sec. III D, except for  $\Delta t_1$  and  $\Delta t_2$ , with descriptions and initial estimates. The parameters which are fitted to data are  $\omega_1^2$ ,  $\omega_{12}^2$ ,  $S_{21}$ ,  $A_{df}$ ,  $A_{sus}$ ,  $\Delta t_1$ ,  $\Delta t_2$ .

Parameter	Description	Note	Estimate
$\omega_1^2, \omega_{12}^2$	parasitic stiffness constants modeling residual oscillatorlike couplings between the SC and the reference TM and between the two TMs	must be estimated from experiments	$\sim 1 \times 10^{-6} \text{ s}^{-2}$
$S_{21}$	sensing cross-talk between $o_1$ and $o_{12}$ interferometric readouts	must be estimated from experiments	$\sim 1 \times 10^{-4}$
$A_{df}, A_{sus}$	actuation gains for the application of forces by the thrusters and the electrostatic suspensions	must be estimated from experiments	$\sim 1$
$\Delta t_1, \Delta t_2$	delays in the application of biases to the controller computing the actuation	must be estimated from experiments	$\leq 1 \text{ s}$
$\Gamma_x$	gravity gradient between the two TMs	could be estimated from experiments with different actuation stiffness, but difficult, considered fixed	$\sim 4 \times 10^{-9} \text{ s}^{-2}$
$m_1, m_2, m_{SC}$	masses of TMs and SC	considered fixed	1.96 kg, 422.7 kg

The model described in this section, with some slight improvements, has been extensively used for simulations and analysis—and examples with references will be discussed in details in the next sections—to test the algorithms aimed at estimating the TM couplings, the sensing cross-talk, and other relevant parameters needed for system calibration. Such calibration is also critical for the unbiased estimation of the total equivalent acceleration noise. The same model is planned to be employed during the identification experiments of the LPF mission.

#### IV. NOISE CHARACTERIZATION

One of the objectives of the LPF mission is to provide a full noise projection of the total equivalent differential acceleration noise between the TMs. As this is well beyond the scope of this paper, the following presents a hint of the problem. Moreover, a theoretical projection of the observed displacement noise is needed in advance in order to identify the dominant effects in the noise and produce the generating filters used for all simulations. The noise projections shown in this section are given by plausible noise shapes implemented in the simulator provided by ESA (which will be specifically introduced in Sec. VID).

Figure 7 shows a projection of the power spectral density (PSD) of the equivalent differential acceleration noise affecting the  $x_{12}$  degree of freedom. A turning point around 6 mHz between two regimes is clearly evident. At high frequency, the  $o_1$  sensing noise dominates the total noise budget. At low frequency, 2/3 of the total noise budget (in units of  $\sqrt{\text{PSD}}$ ) is due to force couplings between the SC and the TMs. Other important noise sources, intervening at low frequency, are the capacitive actuation noise on the second TM, forces on the TMs coming from outside the SC, and the  $o_{12}$  and  $o_1$  sensing noises.

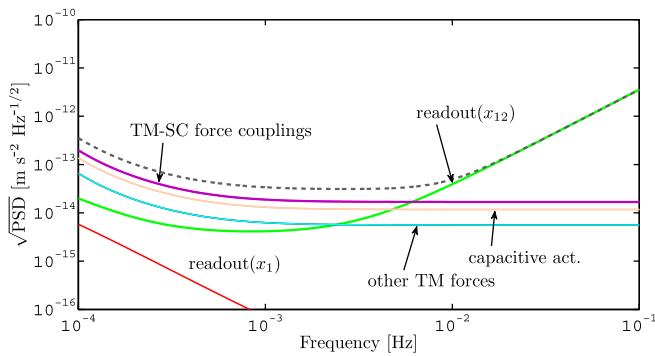


FIG. 7 (color online). Theoretical noise projection of the residual equivalent acceleration noise of the relative motion between the TMs for the nominal dynamics along  $x$ . At high frequency, the  $o_{12}$  sensing noise dominates the total noise budget (dashed line). At low frequency, 2/3 of the total noise budget is due to force couplings between the SC and the TMs. Other important noise sources are the capacitive actuation noise on the second TM, forces on the TMs coming from outside the SC and the  $o_{12}$  and  $o_1$  sensing noises.

The calibration of the system is needed in advance to properly estimate such an acceleration noise shape. In fact, since each single contribution is parameter-dependent, a systematic in a recovered parameter introduces a systematic in the estimated noise, as in Sec. VII.

The above acceleration noise projections are the equivalent acceleration inputs to LPF coming from reasonable noise shapes, producing a characteristic output in the interferometric readouts.

The noise shapes of the interferometric readouts (with their cross-correlation) are also used for simulation purposes. From those models, noise shaping filters are derived and integrated into a multichannel cross-correlated noise generator [22]. Figure 8 reports an example of a noise run lasting 12 hours and obtained by coloring an input zero-mean  $\delta$ -correlated (white) Gaussian noise with those filters.  $o_{12}$  shows a huge red component caused by the increase of the PSD at low frequency, due to forces on the TMs. While  $o_1$  is dominated by the thruster jitter,  $o_{12}$  becomes much less noisy at high frequency, being dominated by readout noise only. The red noise shape of  $o_{12}$  is an expected feature during the experiments of the LPF mission.

In many experiments, and also for LPF, it is a common practice assuming that the noise is stationary all along a measurement. However, it is worth it to stress that in LPF, the noise is parameter-dependent and a nonstationarity in any of the system parameters, which implies a nonstationarity in the noise. In fact, if  $o = o(t, p(t))$  is a generic interferometer readout depending, for simplicity, on just one parameter fluctuating of  $\delta p$  around the nominal value  $p_0$ , then to first order,  $o \simeq o_0 + o' \delta p$ , where  $o_0 = o(t, p_0)$  and  $o' = \partial o(t, p) / \partial o|_{p_0}$ . For a zero-mean process, the total variance is

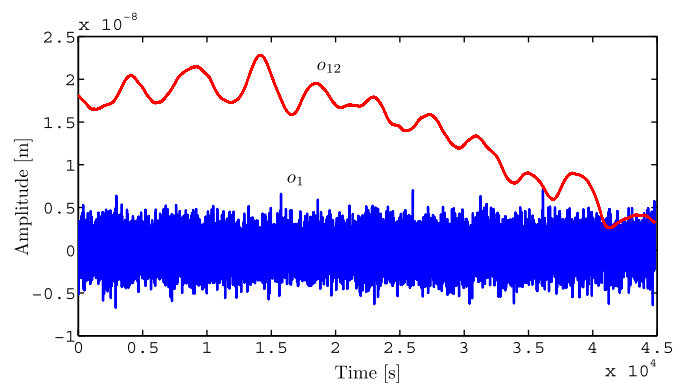


FIG. 8 (color online). A simulated noise run of about 12 hours.  $o_1$  and  $o_{12}$  are the two interferometer readings. Notice the behavior of  $o_{12}$  at low frequency—an expected feature during the LPF mission—showing a huge red component caused by force couplings between the TMs and the SC. At high frequency,  $o_{12}$  becomes much less noisy than  $o_1$ , the former being dominated by only interferometer readout noise and the latter by thruster noise.

$$\text{Var}[o] \approx \text{Var}[o_0] + \text{Var}'[o_0]\delta p + \text{Var}[o']\delta p^2, \quad (20)$$

where the linear and quadratic terms come from the covariance between  $o_0$  and  $o'$  and the variance of  $o'$  itself (see Appendix A for details). Therefore, if any of the system parameters fluctuates, noise is likely to become nonstationary. In LPF, all PSDs must be estimated [23] piecewise along data segments approximately stationary on a time scale given by the one of the fluctuating parameters. The converse, i.e., a nonstationarity in the noise, implies a nonstationarity in any of the parameters is not assured, since other effects, independent from those parameters, may still be relevant. For example, Sec. VIF describes the possibility of existence of glitches, a nonstationary behavior in the noise, and its impact to system identification. More advanced methods, like the time-frequency analysis, are currently under investigation.

## V. IDENTIFICATION EXPERIMENTS

Among the series of experiments characterizing the LPF mission, a few of capital importance will tackle system identification. This paper considers two experiments which are sufficient for a complete identification of the 7 most important system parameters introduced in Sec. II. As said, considering bias injections at the level of controller guidance signals is completely equivalent to applying direct force stimuli through the equivalence given by Eq. (6). In the nominal  $x$  dynamics, two experiments are defined:

- (1) an injection into the controller guidance of the  $o_1$  channel, namely,  $o_{i,1}$ , producing forces on the SC through thruster actuation;
- (2) an injection into the controller guidance of the  $o_{12}$  channel, namely,  $o_{i,12}$ , producing forces on the second TM through capacitive actuation.

The  $o_1$  channel is dominated by the control for almost the entire frequency band, in order to attenuate the SC jitter. For this reason, injecting a signal into  $o_{i,1}$  (i.e., applying a thruster actuation on the SC) allows for the identification, in turn, of the actuation gain,  $A_{\text{df}}$ ; the first TM coupling to the SC,  $\omega_1^2$ ; as well as a possible delay in the application of the same bias,  $\Delta t_1$ .

Analogously, as the  $o_{12}$  channel is dominated by control at low frequency and sensing at high frequency, injecting a signal into  $o_{i,12}$  (i.e., applying a capacitive actuation on the second TM) allows for the identification, in turn, of the actuation gain,  $A_{\text{sus}}$ ; the differential coupling between the TMs,  $\omega_{12}^2$ ; as well as a possible delay in the application of the same bias,  $\Delta t_2$ . Given the cross-talk elucidated in Fig. 6 at low frequency, the sensing cross-talk,  $S_{21}$ , can also be determined.

As the SC motion is common-mode and the first and differential channel are correlated, the estimation of the differential acceleration noise cannot be performed independently of the first channel, which is the only means by

which the SC jitter can be measured and subtracted. The details of such an estimation will be given in Sec. VII.

The next section is devoted to the estimation of the 7 system parameters by means of a MIMO approach which maximizes the overall information. The identification experiments defined at the beginning of this section are simulated for a total duration of almost 3 hours each—a suitable time scale for the mission—by injecting stimulating biases. The following facts are assumed:

- (1) the noise  $\mathbf{o}_n$  is generated as in Sec. IV, independently from the noise-only run which is used for noise characterization, and is Gaussian and stationary;
- (2) the signals  $\mathbf{o}_s$  are simulated in time domain with a MIMO approach by means of Eq. (9b), i.e., by anti-Fourier transforming [26] with  $\mathcal{F}^{-1}$  the deterministic input signals

$$\mathbf{o}_s(t, \mathbf{p}_{\text{true}}) = \mathcal{F}^{-1}[\mathbf{T}_{o_i \rightarrow o}(\omega, \mathbf{p}_{\text{true}})\mathbf{o}_i(\omega)](t), \quad (21)$$

where  $\mathbf{p}_{\text{true}}$  is the set of assumed *true* system parameter values to be estimated from the analysis and on which the estimation of residual equivalent acceleration noise depends;

the superposition principle of signals and noise holds true in the hypothesis of small motion and in the absence of nonlinearities in the system, so that the “experimental” data are simulated by

$$\mathbf{o}_{\text{exp}} = \mathbf{o}_s + \mathbf{o}_n. \quad (22)$$

The underlying idea in parameter estimation is to excite the system with proper high signal-to-noise-ratio (SNR) signals so that the modeled parameters can be measured. A typical injected bias is a series of sine waves of logarithmically increasing frequency, with integer number of cycles, divided by gaps of 150 s to allow for system relaxation. The sine stretches last 1200 s each. The amplitudes are conservatively selected not to exceed 1% of the operating range of the interferometer, corresponding to a maximum sensed displacement of 1  $\mu\text{m}$ , and 10% of the maximum allowed force authority, corresponding to 10  $\mu\text{N}$  of thruster actuation and 0.25 nN of capacitive actuation. The biases are parametrized in Table V and referred to as the *standard input signals* used for the rest of the analysis.

Data are simulated at 10 Hz and decimated to 1 Hz to ease data processing. During the mission, data will be collected at a sample rate between 1 and 10 Hz, depending on the experiment and available down-link bandwidth. The simulation of the first experiment, with injection of the  $o_{i,1}$  signal of Table V, is shown in Fig. 9. The response of the system in  $o_1$  is approximately equal to  $o_{i,1}$ , except at high frequency where there is a modest gain due to the particular shape of the first diagonal element of the transfer function at that frequency. A residual signal in  $o_{12}$  of absolute peak  $\sim 4 \times 10^{-8}$  m is also visible and due to

TABLE V. Controller guidance signals injected as biases for system identification. The sine stretches last 1200 s each and are separated by gaps of 150 s. The sine waves perform an integer number of cycles, from 1 to 64. The amplitudes are selected to not exceed 1% of the operating range of the interferometer and 10% of the maximum force authority.

$o_{i,1}$ for Experiment 1		$o_{i,12}$ for Experiment 2	
$f$ [mHz]	$a$ [ $\mu\text{m}$ ]	$f$ [mHz]	$a$ [ $\mu\text{m}$ ]
0.83	1.0	0.83	0.80
1.7	1.0	1.7	0.48
3.3	1.0	3.3	0.19
6.6	1.0	6.6	0.088
13	0.59	13	0.096
27	0.28	27	0.18
53	0.14	53	0.46

dynamical cross-talk. As said before, the gaps allow for system relaxation, particularly at high frequency.

The simulation of the second experiment, with injection of the  $o_{i,12}$  signal of Table V, is shown in Fig. 10. The response of the system in  $o_{12}$  is evidently phase delayed to  $o_{i,12}$ . At high frequency, the very low gain of the transfer function almost suppresses the signal. Since the transfer from  $o_{i,12}$  to  $o_1$  is negligible, in this experiment,  $o_1$  has signal contribution completely hidden by noise. For this reason, during the mission, the  $o_1$  readout will serve as a useful sanity check for a first understanding of the model.

## VI. SYSTEM IDENTIFICATION

During the mission, noise runs will be used to characterize the noise itself and estimate the total equivalent input acceleration. The estimation of the total equivalent accel-

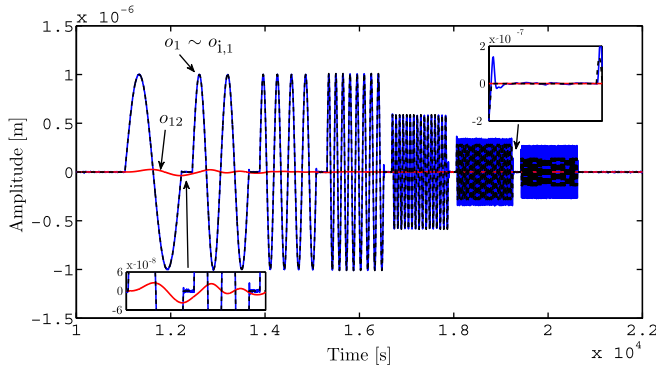


FIG. 9 (color online). Experiment 1 synthetic data. An injection of sine-wave signals lasting for almost 3 hours into the first controller guidance  $o_{i,1}$  produces a different response in the two interferometer readings. The response in  $o_1$  is approximately equal to  $o_{i,1}$  (dashed line), except at high frequency where there is a modest gain. A residual signal in  $o_{12}$  of absolute peak  $4 \times 10^{-8}$  m is due to dynamical cross-talk (see inset at the left bottom side). Gaps between two cycles of injection allow for system relaxation (see inset at the right top side).

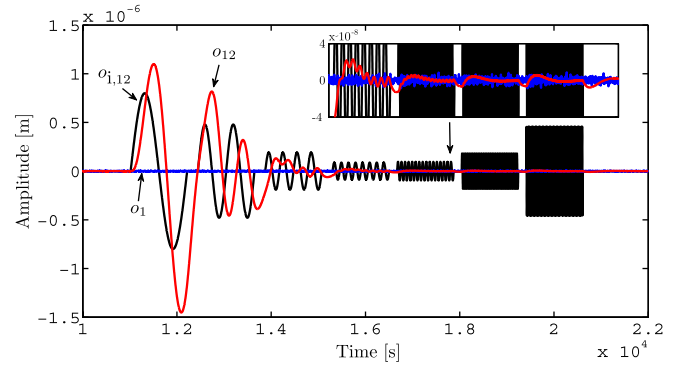


FIG. 10 (color online). Experiment 2 synthetic data. An injection of sine-wave signals lasting for almost 3 hours into the second controller guidance  $o_{i,12}$  produces a different response in the two interferometer readings. The response in  $o_{12}$  is evidently phase delayed to  $o_{i,12}$ . At high frequency, the very low gain of the transfer function almost suppresses the signal (see inset). The  $o_1$  data channel has negligible contribution hidden by the noise.

eration is possible if LPF is properly modeled. For this in the various experiments, signals will be injected along different degrees of freedom to study the response of the system. Along the optical axis  $x$ , LPF will be characterized giving, as a first approximation, the nominal dynamics. Instead, along others degrees of freedom, LPF will be characterized in terms of the many cross-talk contributions arising from the dynamical couplings, the imperfections in the sensing conversion, and the imperfections in the actuation.

This section handles the general problem of estimating the LPF parameters modeled as a MIMO dynamical system, where different inputs enter into the system and produce a response in different outputs. For the sake of simplicity, only the two experiments introduced above—the characterization of the nominal dynamics along  $x$ —are considered for the rest of the paper, bearing in mind that the method is general enough to handle more sophisticated experiments, like the cross-talk from other degrees of freedom to  $x$ . An example would be the identification of the  $xy$  cross-talk, in which guidance or force bias signals are injected, in turn, along  $y_1$ ,  $y_2$ ,  $\phi_1$ ,  $\phi_2$ , and  $\phi_{SC}$  to study the response along the optical axis—the focus of future investigations.

Finally, this section develops and validates the estimation procedures on the two most important experiments described in the previous section. It also shows the application to a couple of nonstandard scenarios which may happen during the real LPF mission.

### A. Review of the problem

The experimental data (either simulated or from the mission) can be modeled superimposing deterministic signals with noise

$$\mathbf{o}_{\text{exp}} = \mathbf{o}_s + \mathbf{o}_n, \quad (23)$$

where  $\mathbf{o}_n$  is the output noise with cross PSD matrix  $\mathbf{S}_n$  and

$$\mathbf{o}_s(t, \mathbf{p}) = \mathcal{F}^{-1}[\mathbf{T}_{o_i \rightarrow o}(\omega, \mathbf{p})\mathbf{o}_i(\omega)](t) \quad (24)$$

are the so-called *template* signals obtained by injecting bias guidance signals  $\mathbf{o}_i$  into the system modeled by the transfer matrix  $\mathbf{T}_{o_i \rightarrow o}$ .

It is useful to think that the experimental data depends on the true parameter values

$$\mathbf{o}_{\text{exp}} = \mathbf{o}_{\text{exp}}(t, \mathbf{p}_{\text{true}}), \quad (25)$$

which need to be estimated from fitting procedures. In the case of simulated experiments, the true values are exactly those used in data generation. In the case of real mission experiments, the true values are actually those giving the best possible description of the data—the one that perfectly subtracts the deterministic signals—hence recovering the instrumental noise shapes.

In the same way, the observed noise (either simulated or from the mission) depends on the parameter values

$$\mathbf{o}_n = \mathbf{o}_n(t, \mathbf{p}_{\text{true}}) \quad (26)$$

but can be considered constant with respect to the parameter values for the time scale of an identification experiment where only high SNR signals will be injected.

The scope of parameter estimation is to recover the best possible description of the experimental data. If the *residuals* between the experimental data and the modeled template signals are defined by

$$\mathbf{o}_r = \mathbf{o}_{\text{exp}} - \mathbf{o}_s, \quad (27)$$

the best possible description of the experimental data is given by

$$\mathbf{o}_r(t, \mathbf{p}_{\text{est}}) \approx \mathbf{o}_n(t, \mathbf{p}_{\text{true}}), \quad (28)$$

implying that the residuals evaluated at the estimated parameter values  $\mathbf{p}_{\text{est}}$  recover the true instrumental noise.

## B. Estimation method

LPF is a MIMO dynamical system for which each experiment has a unique set of meaningful parameters. Hence, for two generic experiments, two sets of parameters can be independently determined. Sometimes a subset may be shared between the two; sometimes there could be parameters which can be estimated by only a particular experiment. Moreover, each experiment has multiple readouts sensitive to different parameters.

The first approach is to build an information-weighted average [20] of different parameter estimates coming from all readouts and experiments. If  $\mathbf{p}_{ij}$  are the parameter estimates of the  $i$ th experiment and  $j$ th readout, the corresponding Fisher information matrix [28]

$$\mathbf{I}_{ij} = \int \nabla_{\mathbf{p}} \mathbf{o}_r^{(ij)}(\omega, \mathbf{p}_{\text{est}})^* \mathbf{S}_n^{(ij)}(\omega)^{-1} \nabla_{\mathbf{p}} \mathbf{o}_r^{(ij)}(\omega, \mathbf{p}_{\text{est}}) d\omega, \quad (29)$$

where  $\mathbf{S}_n^{(ij)}$  is the noise PSD of  $i$ th experiment and  $j$ th readout,  $\mathbf{o}_r^{(ij)}$  is the corresponding vector of residuals,  $\nabla_{\mathbf{p}}$  is the gradient with respect to the parameters, and  $*$  is the conjugate transpose. The final combined parameter estimates are given by

$$\mathbf{p} = \mathbf{I}^{-1} \sum_{i=1}^{N_{\text{exp}}} \sum_{j=1}^{N_o} \mathbf{I}_{ij} \mathbf{p}_{ij}, \quad (30)$$

where  $N_{\text{exp}}$  is the number of experiments and  $N_o$  the number of readouts per experiment assumed the same across the experiments. The combined Fisher information matrix is

$$\mathbf{I} = \sum_{i=1}^{N_{\text{exp}}} \sum_{j=1}^{N_o} \mathbf{I}_{ij}. \quad (31)$$

Notice that the estimates  $\mathbf{p}_{ij}$  may have different dimension depending of the  $i$ th experiment and  $j$ th interferometric readout; the same happens for the corresponding information matrices. The issue can be easily solved by inserting zeroes where there is no information.

An example can readily show that the definition of Eq. (30) is not robust. In fact, suppose that the estimation of the system parameters is performed independently on each readout and one of those parameters has a biased value for an inaccuracy of the transfer matrix model. Therefore, the information matrix for that estimate is biased, and the combined one in Eq. (31) is as well. The numerical inversion in Eq. (30) inexorably amplifies that bias to the combined parameter estimates. To overcome the problem, one could try removing the failing estimates (which is possible only if one has good indication of what the real values are, for example, from ground measurements or previous independent experiments), but in doing so, information and precision would definitely be lost.

The only solution is to attack the problem by a complete MIMO approach where the poor information coming from the biased model of a readout is continuously compensated by the others as the optimization goes on. One other advantage is that a joint information can likely remove or, at least, reduce the effect of parameter degeneracies.

The MIMO-multiexperiment joint log-likelihood of the system is a generalization of the standard definition [28] and is given by

$$\chi^2(\mathbf{p}) = \int \mathbf{o}_r(\omega, \mathbf{p})^* \mathbf{S}_n(\omega)^{-1} \mathbf{o}_r(\omega, \mathbf{p}) d\omega, \quad (32)$$

where

$$\mathbf{o}_r(\omega, \mathbf{p}) = \mathbf{o}_{\text{exp}}(\omega) - \mathbf{T}_{o_i \rightarrow o}(\omega, \mathbf{p})\mathbf{o}_i(\omega) \quad (33)$$

are the residuals between the experimental data  $\mathbf{o}_{\text{exp}}$  and the modeled system response.  $\mathbf{o}_i$  are the controller biases,  $\mathbf{T}_{o_i \rightarrow o}$  is the transfer matrix depending on all system parameters  $\mathbf{p}$  (stiffness constants, sensing cross-talk, etc.), and  $\mathbf{S}_n$  is the cross output noise PSD matrix assumed constant to the system parameters. For two experiments and two interferometric readouts each,  $\mathbf{o}_i$  is a 4-vector, null in the second and third element, since the injection is in  $o_{i,1}$  (first experiment) and  $o_{i,12}$  (second experiment);  $\mathbf{T}_{o_i \rightarrow o}$  is a block diagonal  $4 \times 4$  matrix replicating the same  $2 \times 2$  matrix;  $\mathbf{S}_n$  is a  $4 \times 4$  matrix of cross PSDs between different readouts and experiments; and  $\mathbf{o}_{\text{exp}}$  is a 4-vector of all experimental readouts.

Assuming that all readouts are sampled at the same rate and last for the same duration, the overall number  $\nu$  of degrees of freedom for the problem is defined as

$$\nu = N_{\text{exp}} \times N_o \times N_{\text{data}} - N_p, \quad (34)$$

where  $N_{\text{exp}}$  is the number of experiments;  $N_o$  is the number of readouts per experiment (assumed the same across the experiments);  $N_{\text{data}}$  is the number of data points per readout;  $N_p$  is the dimension of the parameter space. For example,  $\nu \sim 4 \times 10^4$  for two experiments, two readouts each, lasting for about 3 hours and sampled at 1 Hz. For the rest, if not otherwise stated, the reduced log-likelihood  $\chi^2/\nu$  will be used in place of the standard definition, as its expectation value is 1.

The MIMO-multiexperiment Fisher information matrix for the parameter estimates  $\mathbf{p}_{\text{est}}$  is the local curvature of the log-likelihood surface around the minimum and is given by

$$I = \int \mathbf{o}_i(\omega)^* \nabla_{\mathbf{p}} \mathbf{T}_{o_i \rightarrow o}(\omega, \mathbf{p}_{\text{est}})^* \mathbf{S}_n(\omega)^{-1} \nabla_{\mathbf{p}} \mathbf{T}_{o_i \rightarrow o}(\omega, \mathbf{p}_{\text{est}}) \mathbf{o}_i(\omega) d\omega, \quad (35)$$

where  $\nabla_{\mathbf{p}}$  is the gradient with respect to all 7 system parameters. As above, if  $\mathbf{T}_{o_i \rightarrow o}$  is a  $4 \times 4$  matrix, then  $\nabla_{\mathbf{p}} \mathbf{T}_{o_i \rightarrow o}$  is a  $7 \times 4 \times 4$  tensor, and the information is a  $7 \times 7$  matrix as required. The very high SNR regime of the signals in Figs. 9 and 10 assures that the linear approximation of Eq. (35) holds true and no corrective terms arise as pointed out by Ref. [29] and more recently by Ref. [30]. As the inverse of the information matrix provides the estimated covariance matrix, the validity of the linear approximation is checked *a posteriori* in Sec. VI E by inspecting the statistics of a Monte Carlo simulation.

### C. Search algorithm

The joint log-likelihood (32) for two experiments, two readouts each, is implemented in time domain by means of the FFT/inverse FFT time series. The relevant iteration steps of the process taking to the final estimates of the system parameters, in loop of increasing accuracy, are

- (1) the whitening filters are estimated on a long noise run, as described in Appendix B;
- (2) the interferometric readouts of each experiment are whitened;
- (3) the templates are generated according to Eq. (24) for the current parameter values;
- (4) the templates are whitened;
- (5) the log-likelihood is evaluated, i.e., “models fit the data”, for the current parameter values;
- (6) the parameter values are updated according to the adopted optimization scheme.

From the optimization viewpoint, the log-likelihood is named the *merit function*, i.e., the one being minimized as the parameter values are updated. Figure 11 shows a sketch of the whole process of system identification. The

data production provides for the noise run and the experiments, with both interferometric readouts and injected biases. Instead, the modeling provides for the proper transfer matrix being used for simulating the template signals. Finally, the data analysis concerns the estimation of the whitening filters and the algorithm for the log-likelihood minimization.

The algorithm performs a log-likelihood minimization by taking advantage of the most recent developments in numerical nonlinear optimization [27]. During this work, an investigation of different optimization algorithms was carried out. Nonstandard schemes like the *simulated annealing*, *genetic algorithms*, and the *pattern search*, with or without a multistart (an initial Monte-Carlo-like exploration of the parameter space in which the initial most likely

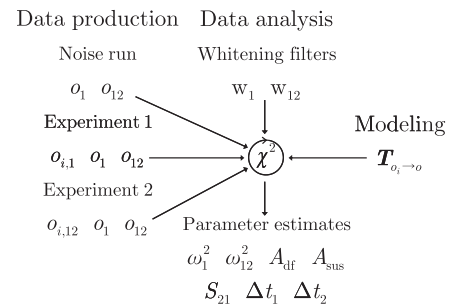


FIG. 11. Sketch of the system identification process for the two simulated experiments along the optical axis. Noise run and experiments pertain to data production. The modeling provides for the transfer matrix being used for simulation and analysis. For system identification, data analysis comprises the estimation of whitening filters and the log-likelihood optimization. The estimated parameters are output together with their covariance matrix.

points are taken into account for further processing), were considered for the purposes of system identification. They were also compared to a mixed strategy employing more standard and widely used optimization algorithms applied in sequence:

- (1) the *preconditioned conjugate gradient search* (alternatively, the quasi-Newton method) explores the parameter space to large scales;
- (2) the *derivative-free simplex* makes it possible to reach the required numerical accuracy.

The key advantage of mixing different approaches is that the global structure of the parameter space can be explored while keeping the numerical accuracy. Such an investigation proved that for the LPF system identification, non-standard schemes have comparable performances with respect to the one proposed above which is assumed for the rest. The optimization is numerically controlled and stopped until either the function tolerance or the average parameter tolerance meets the requirement of  $1 \times 10^{-4}$ . The final parameter estimates are output from the fitting tool, together with the estimated covariance matrix, obtained by inverting the Fisher information matrix (35) around the minimum.

#### D. ESA simulator

A very important test bench on both system modeling and validation of the estimation techniques is the analysis of realistic data, closer to the actual LPF mission than the ones simulated and shown in this work. A real LPF offline simulation environment, provided by ESA and written by ASTRIUM has given the chance to promptly analyze the data as they were realistically produced during the mission. The simulator is a state-space representation of a 3-dimensional LPF model written under the MATLAB and SIMULINK [31] environments. It contains the most relevant disturbances and noise sources, the same actuation algorithms for drag-free, electrostatic suspension and attitude controls embedded in LPF, all couplings within the dynamics along the optical axis and between different

degrees of freedom. The simulator was written to mainly check all procedures, the mission timeline, the experiments, and to validate the noise budget.

Several extended data-analysis operational exercises were performed in the past 2 years. Parameter estimation had a central role, and data production was strictly separated from data analysis. The operational exercises culminated with the comparison of the three parameter-estimation methods: a linear fit with singular value decomposition, a Markov-chain Monte Carlo method, and the one described in Ref. [8]. The final conclusion of the activity on the same exercise is recently described in Ref. [32]. The three methods are apparently in good agreement with each other, particularly the first and third approaches, but an investigation of the fit residuals, like the one in Fig. 18, shows a mismatch in the first experiment between data and model at high frequency. The fact is confirmed by a statistical comparison between the residual PSDs to a noise-only measurement with a very general and model-independent method based on the Kolmogorov-Smirnov test [33].

#### E. Monte Carlo validation

The aim of this section is to statistically validate the estimation method presented so far. A Monte Carlo simulation of 1000 different noise realizations is used to check for consistency of the method. The estimation is identically repeated at each step, enabling fine tuning and the study of the statistics for every system parameter.

Table VI reports on the comparison between the mean best-fit values and the true values: the accordance is at the level of, at most, 2 standard deviations and demonstrates that the estimation method is statistically unbiased. Secondly, it shows the best-fit standard deviations, i.e., the parameter fluctuations due to noise, compared to the mean expected standard deviations (the mean fit errors).

Figure 12 shows a more in-depth analysis of all parameter statistics. The accordance between the sample statistics of the Monte Carlo simulation and the scaled theoretical Gaussian probability density function (PDF) (evaluated at

TABLE VI. Monte Carlo validation of 1000 independent noise realizations on which parameter estimation is repeated identically at each step. The mean best-fit values are compatible with the true values within 2 standard deviations. The terms in brackets are the error relative to the right-most digit. The mean expected standard deviations (estimated from the fit) and the best-fit standard deviations are approximately the same order of magnitude. The mean log-likelihood is  $\chi^2 = 0.96$  with  $\nu = 79993$ .

Parameter	True	Mean best-fit	Best-fit standard deviation	Mean expected standard deviation
$\omega_1^2$ [ $10^{-6} \text{ s}^{-2}$ ]	-1.303	-1.303006(7)	$2 \times 10^{-4}$	$1 \times 10^{-3}$
$\omega_{12}^2$ [ $10^{-6} \text{ s}^{-2}$ ]	-0.698	-0.697998(6)	$2 \times 10^{-4}$	$5 \times 10^{-4}$
$S_{21}$ [ $10^{-4}$ ]	0.9	0.90004(9)	$3 \times 10^{-3}$	$4 \times 10^{-3}$
$A_{df}$	1.003	1.00297(1)	$4 \times 10^{-4}$	$4 \times 10^{-4}$
$A_{sus}$	0.9999	0.9999001(1)	$4 \times 10^{-6}$	$2 \times 10^{-5}$
$\Delta t_1$ [s]	0.06	0.059995(3)	$9 \times 10^{-5}$	$3 \times 10^{-4}$
$\Delta t_{12}$ [s]	0.05	0.05000(3)	$8 \times 10^{-4}$	$1 \times 10^{-3}$

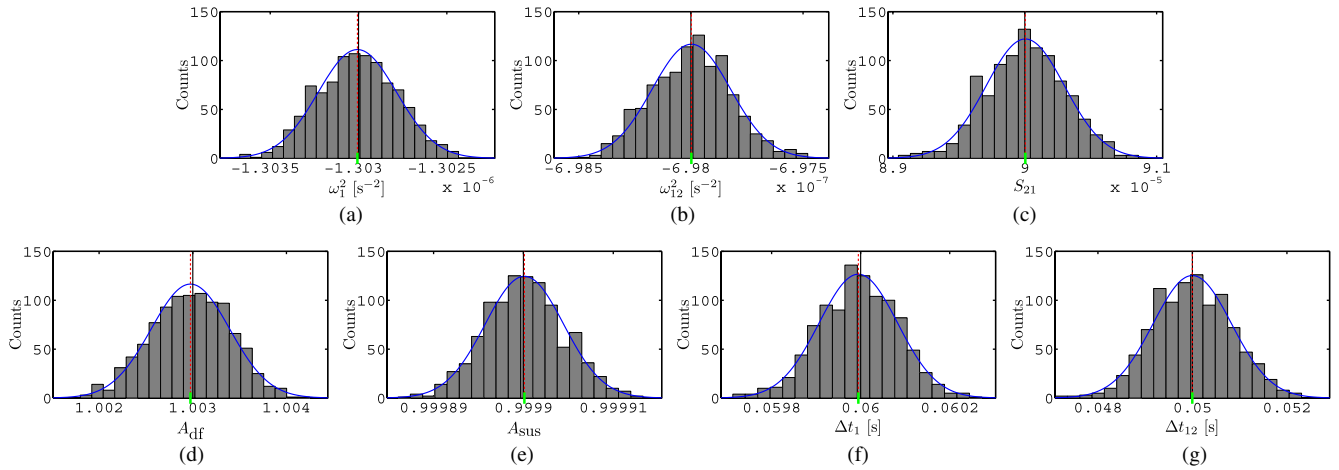


FIG. 12 (color online). Monte Carlo validation of 1000 independent noise realizations on which parameter estimation is repeated identically at each step. The plots show the statistics for all parameter estimates (a)–(g). The scaled Gaussian PDF is evaluated at the sample mean (dashed vertical lines) and sample standard deviation (half horizontal bars), which are compared to the true values (solid vertical lines).

the sample mean and standard deviation) is self-evident and demonstrates that: (i) the estimation is statistically unbiased, and (ii) the parameters are Gaussian-distributed.

Analogously, Fig. 13 shows the statistics for the estimated variances. Theory prescribes that the variance must be  $\chi^2$ -distributed, but for  $\nu = 79993$ , the  $\chi^2$  distribution tends to a Gaussian distribution with very good approximation, as is clear from the plots.

Appendix C also discusses some other interesting features of the Monte Carlo statistics, like the parameter correlation, related to the rotation of the log-likelihood paraboloid principal axis around the minimum, and the scatter of the estimation chains due to the noise fluctuation.

The final, and most remarkable check, is the comparison between the fit  $\chi^2$  log-likelihood and the one calculated on

pure noise data contained in Fig. 14. It is worth stressing that both the fit and the noise  $\chi^2$  showed agreement between each other, but they were both positively skewed in a preliminary Monte Carlo simulation. The following facts explain why. Appendix B discusses the practical method to implement the diagonalization of the noise covariance matrix with its main limitation. This consists of the impossibility of filtering out the lowest frequencies, due to the finiteness of the data stretches from which whitening filters are derived and which causes the skewness. Transparently, the application of a high-pass filter to the data has solved the issue. The comparison in the plot provides for an important twofold test: on one side, the parameter variances are statistically distributed as the fit  $\chi^2$  log-likelihood, as required; on the other, the fit  $\chi^2$  log-likelihood is in agreement with the noise  $\chi^2$  log-likelihood, showing that

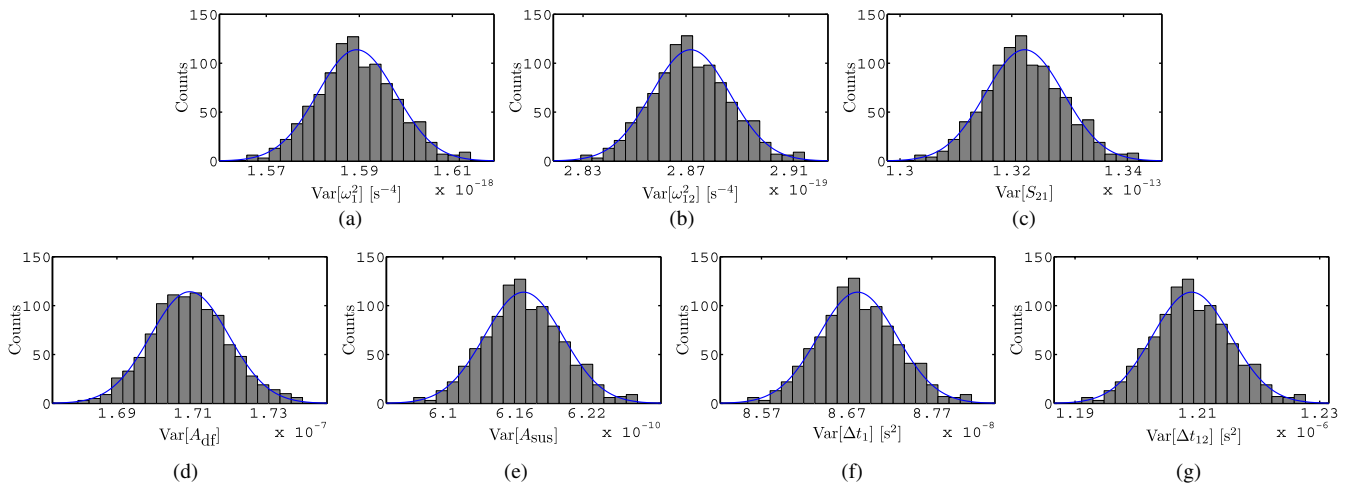


FIG. 13 (color online). Monte Carlo validation of 1000 independent noise realizations on which parameter estimation is repeated identically at each step. The plots show the statistics for all parameter variances (a)–(g). The scaled Gaussian PDF is evaluated at the sample mean and standard deviation.

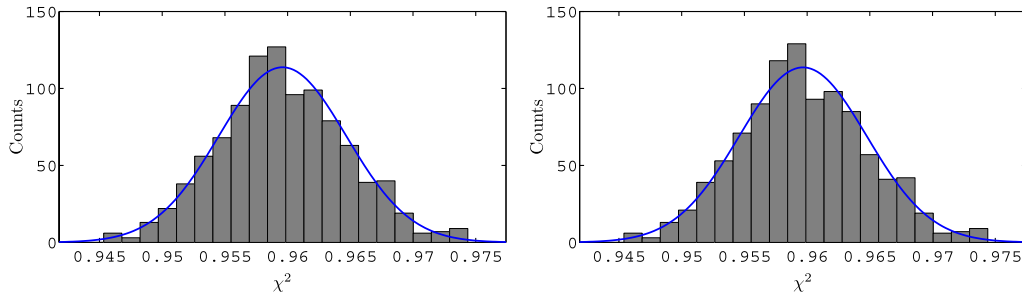


FIG. 14 (color online). Monte Carlo validation of 1000 independent noise realizations on which parameter estimation is repeated identically at each step. The plots show the statistic for (a) the fit  $\chi^2$  log-likelihood and (b) the noise  $\chi^2$  log-likelihood. The agreement between the two demonstrates that the deterministic signals are statistically suppressed out of the data.

the estimation method has statistically suppressed the deterministic signals and recovered the noise statistic with no extra bias.

### F. Nonstandard scenario: non-Gaussianities

This section is devoted to showing the impact of noise non-Gaussianities on parameter estimation. The main realistic behavior of experimental noise is the possible presence of outliers; consequently, the sampling distribution of the data may show some prominent tails. An example of such outliers is the manifestation of glitches, very short noise transients due to anomalous response in the readout/circuitry.

Given the non-Gaussian components in the noise, the log-likelihood defined so far is no longer well-behaved. Because of the intrinsic assumption of Gaussianity, it usually overweighs the outliers, and a systematic error may arise. A standard approach, named *local L estimate* [27], requires the generalization of the definition of log-likelihood. The idea is to properly take care of the outliers by regularizing the usual square of whitened residuals with other similar definitions by means of a weighting function  $\rho$ ,

$$\chi^2 = \sum_i \rho(r_{w,i}), \quad (36)$$

where, as an example, three possible choices (the squared, absolute, and logarithmic deviations) are considered:

$$\rho(r_{w,i}) = \begin{cases} r_{w,i}^2 & \text{mean squared dev.} \\ |r_{w,i}| & \text{mean absolute dev.} \\ \log(1 + r_{w,i}^2) & \text{mean logarithmic dev.} \end{cases}, \quad (37)$$

corresponding to the cases of data distributed according to Gaussian, log-normal, and Lorentzian distribution, respectively. The subscript  $i$  is a generalized index counting the data available from all experiments and interferometric readouts, and  $r_{w,i}$  is the whitened time series of residuals. Figure 15 compares the three weighing functions for residuals out to 5 standard deviations. As is clear, the squared deviation overweighs the outliers. The absolute deviation gives a slightly better weight at high deviations, but per-

forms poorly at low deviations. The logarithmic deviation has much more flexibility as it behaves like the squared deviation at low deviations and performs better than the absolute deviation.

The method can be successfully applied to data with glitches. Noise glitches are unpredictable high-frequency noise transients mostly due to failures in the circuitry. Such outliers usually fall well beyond 3 standard deviations and produce an excess at the tails of the statistic. Since the output of the interferometer might be subject to similar phenomena, this section presents the results of the investigation of a realistic experiment containing glitches. Such transients are modeled as sine-Gaussian functions,

$$o_{\text{gl}}(t) = a \sin[2\pi f_0(t - t_0)] \exp\left[-\frac{(t - t_0)^2}{\tau^2}\right], \quad (38)$$

where the glitch parameters span a wide (uniformly distributed) range of values. In particular, the glitch frequency,  $f_0$ , covers the whole bandwidth ( $10^{-4} - 0.45$ ) Hz; the injection time,  $t_0$ , is distributed all along the time series; the characteristic time,  $\tau$ , giving the typical duration of the pulse is (1–2) s; and the amplitude,  $a$ , falls outside the Gaussian statistic by (3–20) noise standard deviations. Moreover, the number of glitch injections is fixed as a

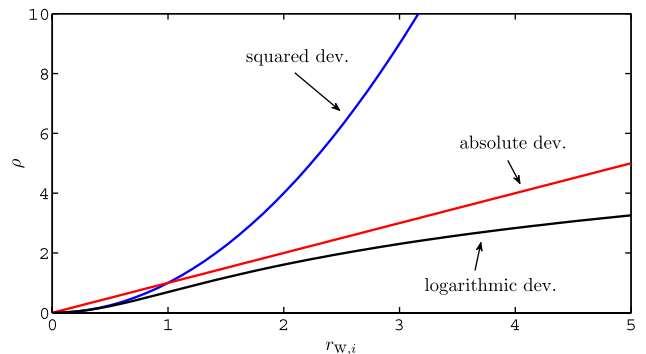


FIG. 15 (color online). Comparison of the three weighing functions of Eq. (37) for the proper weighing of outliers in the data. The logarithmic deviation is the most accurate as it behaves like the squared deviation at low deviations and performs better than the absolute deviation.

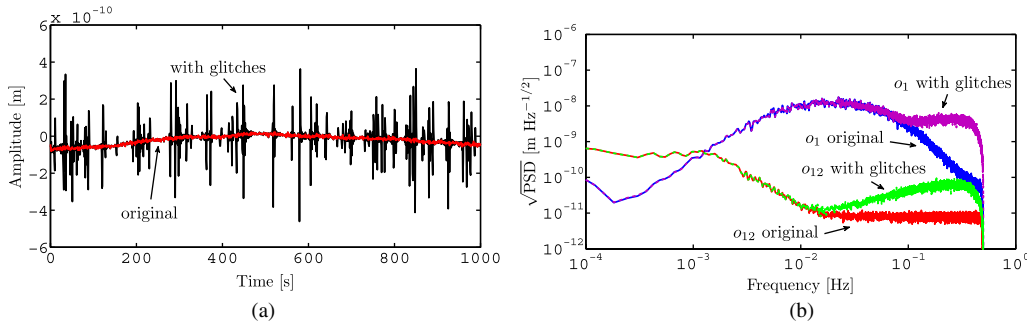


FIG. 16 (color online). Robustness to a nonstandard scenario: non-Gaussianities. (a) simulated original and glitchy noise for  $o_{12}$ ; (b) PSDs of the simulated original and glitchy noise for  $o_1$  and  $o_{12}$ . The level of data corruption is evident and glitches appear as high-frequency bumps around 0.2 Hz.

fractional part of the whole data series, conventionally choosing  $f_{\text{gl}} = N_{\text{gl}}/N_{\text{data}} = 1\%$ , since higher values are very unlikely. Notice that this value represents only the number of injections: the actual fraction of corrupted data is the order of  $3E[\tau]f_{\text{gl}} \simeq 5\%$ .

Glitchy noise is readily produced by coloring a white, zero-mean, unitary standard deviation input time series, as in Sec. IV, corrupted by random injections of glitches. Figure 16 shows how glitches appear in the interferometric differential readout and in the estimated PSDs, compared to the original noise stretches. The effect of glitches is that the PSD of the simulated noise scales linearly with the frequency, up to  $4 \times 10^{-9} \text{ m Hz}^{-1/2}$  and  $6 \times 10^{-11} \text{ m Hz}^{-1/2}$  around 0.2 Hz for the first and differential readout, respectively. This excess noise sums up to the original one and is shown as high-frequency components. Obviously, the noise statistic contains an excess at the tails. For example,  $o_1$  has an excess kurtosis of  $\sim 19$ , compared to the original one of  $-9 \times 10^{-3}$ . No significant difference in skewness is detected since the statistic does not lose symmetry with the glitch injections.

Whitening filters are derived from the glitchy noise stretches with the same procedure described in Appendix B. However, since the whitening process works assuming stationarity, glitches are not filtered out from the data.

Table VII shows the results of three different parameter estimations with the definitions of the weighting functions in Eq. (37). The most conservative least square estimator provides overestimated errors since they scale as  $\sim \sqrt{\chi^2}$ . The absolute and logarithmic deviations provide better statistics and lower errors, but the first gives biased estimates of  $A_{\text{sus}}$ ,  $\Delta t_1$ , and  $\Delta t_{12}$ , and the last one a slightly biased estimate of  $S_{21}$ . The analysis of residuals demonstrates that the three methods recover the noise shapes and are in agreement with each other, so the systematic errors are only in the estimated parameters. These estimators are also 30% and 9% faster than the Gaussian (mean squared deviation), as the outliers have less influence on the estimation chains.

By inspecting the results, it turns out that there is no absolute rule which can be applied when dealing with glitches. However, from the differences between the estimates it is possible to infer the sensitivity of each single parameter to glitches. For example, adopting the ratio between the biases as the *a posteriori* criterion for comparing two methods, it tends to one if that parameter is not sensitive to glitches; otherwise, it tends to a very small or very large number. In view of this consideration, the comparison between the mean squared deviation and the mean logarithmic deviation gives that  $S_{21}$  is the most sensitive parameter, whereas  $\Delta t_{12}$  is the least.

TABLE VII. Robustness to a nonstandard scenario: non-Gaussianities. The comparison between three parameter estimations with the three definitions in Eq. (37).  $\nu = 79193$ . The term in brackets is the error relative to the right-most digit. In curly brackets, the bias (absolute deviation from the real value in units of standard deviation) for each estimate.

Parameter	Real	Best-fit (mean squared deviation) $\chi^2 = 10$		Best-fit (mean absolute deviation) $\chi^2 = 2.1$		Best-fit (mean logarithmic deviation) $\chi^2 = 0.95$		Guess
$\omega_1^2 [10^{-6} \text{ s}^{-2}]$	-1.32	-1.320(1)	{0.061}	-1.3188(6)	{2.0}	-1.3192(4)	{2.0}	-1.3
$\omega_{12}^2 [10^{-6} \text{ s}^{-2}]$	-0.68	-0.6798(7)	{0.29}	-0.68000(3)	{0.011}	-0.6804(2)	{1.8}	-0.7
$S_{21} [10^{-4}]$	1.1	1.10(2)	{0.074}	1.113(7)	{1.8}	1.116(5)	{3.4}	0
$A_{\text{df}}$	1.01	1.011(3)	{0.29}	1.010(1)	{0.23}	1.0109(8)	{1.2}	1
$A_{\text{sus}}$	0.99	0.99000(5)	{0.035}	0.98959(2)	{20}	0.99001(1)	{0.99}	1
$\Delta t_1$ [s]	0.1	0.100(3)	{0.045}	0.090(1)	{8.3}	0.1007(8)	{0.90}	0
$\Delta t_{12}$ [s]	0.1	0.098(5)	{0.36}	-0.0290(2)	{58}	0.098(2)	{1.2}	0

Starting from the fact that the three methods give the same results for purely Gaussian noise, a proposed recipe is the following:

- (1) apply the conservative approach (the ordinary mean squared deviation) directly to corrupted time series and try with different estimators (mean absolute deviation, mean logarithmic deviation, etc.);
- (2) start removing some outliers, giving them negligible weight;
- (3) redo the analysis with all estimators;
- (4) check for convergence and agreement between the estimators.

The overall process can be actually viewed as a reweighing analysis providing for robust uncertainties and, at the same time, the removal of outliers in a step-by-step smooth readjustment. Even though it would be possible, in principle, to clean up the data just before the estimation, in that case, the results would likely be dependent on the statistical criterion used for such cleaning. Even though it is beyond the scope of this paper to implement the idea, it is worth observing that the two main advantages of the preceding recipe are its robustness in definition and the fact that data polishing is smooth and model-independent.

### G. Nonstandard scenario: underperforming actuators and underestimated couplings

System identification has a key role in compensating the SC jitter and the TM couplings. Even in the unlikely (but possible) situation of underperforming actuators or underestimated force couplings, it is still possible to retrieve the actual parameter values and allow for a precise estimation of the total equivalent acceleration noise without losing sensibility and getting into systematic errors. The impact on the estimation of the total equivalent acceleration noise will be illustrated in Sec. VII.

To introduce the problem, suppose that the predicted TM couplings are  $\omega_1^2 = -1.3 \times 10^{-6} \text{ s}^{-2}$  and  $\omega_{12}^2 = -0.7 \times 10^{-6} \text{ s}^{-2}$ , and during the LPF mission:

- (1) the actual TM couplings are about 2 times the predicted ones, due to unexpected/unmodeled stronger forces, like  $\omega_1^2 = -3 \times 10^{-6} \text{ s}^{-2}$  and  $\omega_{12}^2 = -2 \times 10^{-6} \text{ s}^{-2}$ ;
- (2) the thruster and capacitive actuators unfortunately malfunction, due to both a breakdown of one or more thruster clusters and a loss of efficiency in the capacitive actuators on the second TM; this situation can be described by gains sensitively lower than one, like  $A_{df} = 0.62$  and  $A_{sus} = 0.6$ ;
- (3) the interferometer introduces an extra cross-talk,  $S_{21} = 1.5 \times 10^{-3}$ , 10 times the expected one  $S_{21} \sim 1 \times 10^{-4}$ .

In this very unfortunate situation, system identification (see Table VIII) allows for the estimation of the true values within 1 standard deviation from the true values, so maintaining precision, even though the optimizations starts from initial guesses which are typically  $\sim 10^3$  standard deviations away, so guaranteeing accuracy too.

Figure 17 elucidates much more the results, showing the overall performances of the estimation. The  $\chi^2$  is reduced from  $1 \times 10^5$  to  $\sim 1$ —the required optimum—within the given tolerances (set to  $1 \times 10^{-4}$  in both log-likelihood and parameter values), while keeping both accuracy and precision. The figure reports two examples of estimation chains (for  $\omega_1^2$  and  $\omega_{12}^2$ ), showing the correlation with the big jumps in the  $\chi^2$  chain and how the parameters saturate to the optimum values. The estimation, as already said, is divided into two phases: a gradient-based search, spanning the global structure of the parameter space, and a simplex search, improving the final accuracy.

The final and most important discussion is the analysis of residuals summarized in Fig. 18 for both identification experiments and interferometric readouts. The estimated PSDs of both initial and best-fit residuals are compared to the PSDs of an independent noise run. It is clear that the deterministic signals are completely subtracted from the data, hence recovering the noise shapes for all experiments and readouts. The improvement is mostly evident at low

TABLE VIII. Robustness to a nonstandard scenario: underperforming actuators/underestimated couplings. Initial estimates (guess) at  $\chi^2 = 1.3 \times 10^5$ ,  $\nu = 79193$ ; best-fit values at  $\chi^2 = 0.99$ . The term in brackets is the error relative to the right-most digit. In curly brackets, the bias (absolute deviation from the real value in units of standard deviation) for each estimate.

Parameter	True	Best-fit		Guess	
$\omega_1^2 [10^{-6} \text{ s}^{-2}]$	-3	-2.9998(2)	{1.1}	-1.3	$\{7.8 \times 10^3\}$
$\omega_{12}^2 [10^{-6} \text{ s}^{-2}]$	-2	-2.0000(1)	{0.32}	-0.7	$\{1.0 \times 10^4\}$
$S_{21} [10^{-3}]$	-1.5	-1.4998(1)	{0.55}	0	$\{4.7 \times 10^3\}$
$A_{df}$	0.62	0.61994(8)	{0.77}	1	$\{4.9 \times 10^3\}$
$A_{sus}$	0.6	0.599990(8)	{1.3}	1	$\{5.1 \times 10^4\}$
$\Delta t_1 [s]$	0.6	0.6013(7)	{1.8}	0	$\{8.4 \times 10^2\}$
$\Delta t_{12} [s]$	0.4	0.398(2)	{0.95}	0	$\{2.3 \times 10^2\}$

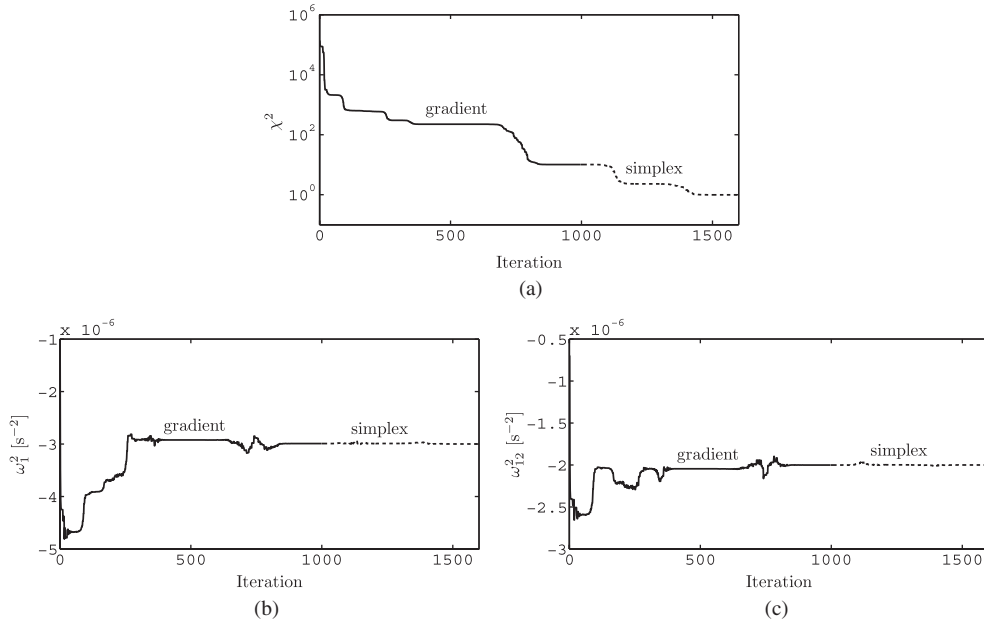


FIG. 17. Robustness to a nonstandard scenario: underperforming actuators/underestimated couplings. The estimation performances relative to the log-likelihood minimization (a) from  $\sim 1 \times 10^5$  to the optimum  $\sim 1$  and two examples of estimation chains for (b)  $\omega_1^2$  and (c)  $\omega_{12}^2$  showing the correlation with the big jumps in the  $\chi^2$  chain. A preliminary global gradient search is followed by a local simplex. The process lasts for 1636 iterations and stops when the required tolerance is met.

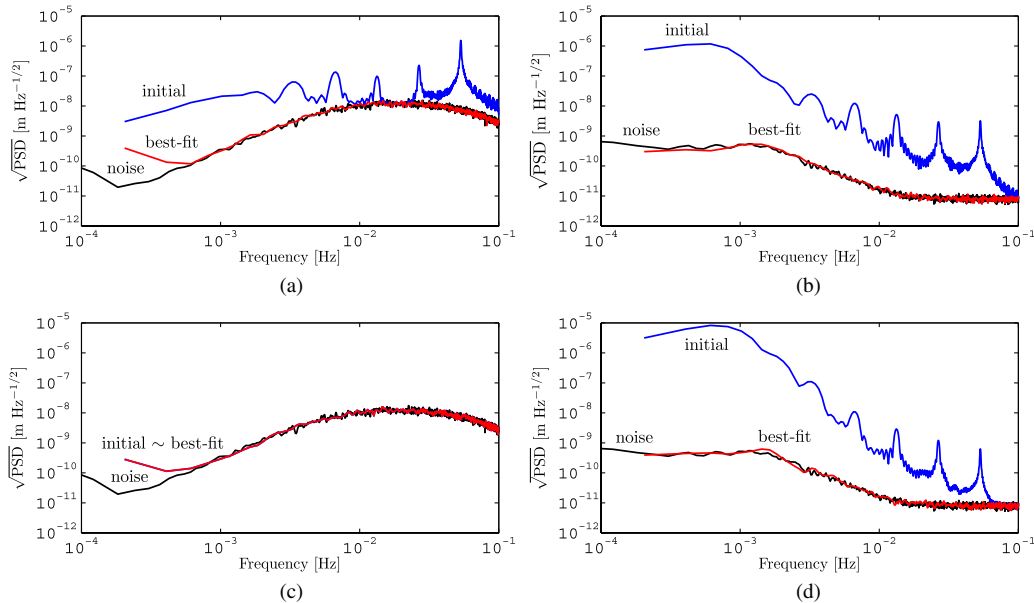


FIG. 18 (color online). Robustness to a nonstandard scenario: underperforming actuators/underestimated couplings. Analysis of residuals for all simulated identification experiments and interferometric readouts. Initial and best-fit residuals are compared to the expected noise shapes estimated from an independent run. For  $o_{12}$ , the improvement in both experiments (b) and (d) is of  $\sim 4$  orders of magnitude around 1 mHz; (a) for  $o_1$  in the first experiment is 3 orders of magnitude; (c) contains no signal.

frequency: for  $o_{12}$  the residuals are suppressed by  $\sim 4$  orders of magnitude around 1 mHz. The same happens for  $o_1$  in the first experiment where the improvement is of  $\sim 2$  orders of magnitude. Only  $o_1$  in the second experiment shows no improvement since the signal is negligible.

### VII. ESTIMATION OF TOTAL EQUIVALENT ACCELERATION NOISE

This section justifies the efforts in developing the techniques introduced so far with all tests and validation runs,

showing the impact of system identification on the estimation of the total equivalent acceleration noise. As said throughout this paper, the main objective of the LPF mission in view of a real GW astronomy with spaced-based detectors is the characterization of the Doppler link of LISA as the fundamental spacetime meter in terms of equivalent differential acceleration. Even if LPF is different in design with respect to LISA—no faraway optical measurement between two SCs is actually implemented—yet the principle and, most of all, the performances in sensitivity can be extrapolated and gather more confidence in the scientific scopes of any spaced-based GW detector.

Assessing the performance in sensitivity as equivalent input acceleration noise is a very effective way to put dynamics, sensing, and control on the same footing. This can be achieved by means of the  $\Delta$  operator of Sec. III C, connecting interferometric displacement readouts to total equivalent acceleration and, at the same time, compensating for TM couplings, SC jitter, and sensing cross-talk.

Suppose that  $S_{n,o}(\omega, \mathbf{p}_{\text{true}})$  is the measured interferometric noise PSD. Then, the estimated total equivalent acceleration noise PSD is given by

$$S_{n,f}(\omega, \mathbf{p}_{\text{est}}) = \Delta(\omega, \mathbf{p}_{\text{est}})S_{n,o}(\omega, \mathbf{p}_{\text{true}})\Delta(\omega, \mathbf{p}_{\text{est}})^*, \quad (39)$$

where  $\Delta(\omega, \mathbf{p}_{\text{est}})$  models the transfer from interferometric displacement readouts to total equivalent acceleration and  $\mathbf{p}_{\text{est}}$  are the parameter estimates as obtained by system identification. It is worth noting that if  $S_{n,o}$  was assumed constant to the parameter values in first approximation, the transfer to total equivalent acceleration would anyhow couple the output noise with the dynamics so that the estimated total equivalent acceleration noise becomes explicitly dependent on the parameter values. This shows that *parameter estimation serves not only for system identification, but also for the actual identification of the total equivalent acceleration noise.*

Furthermore, suppose that  $\mathbf{p}_{\text{est}} \simeq \mathbf{p}_{\text{true}} + \delta\mathbf{p}$ , with  $\delta\mathbf{p}$  the parameter biases being much larger than the statistical uncertainties on  $\mathbf{p}_{\text{est}}$ . It is easy to show that the parameter biases propagate to the differential operator  $\Delta_{\text{est}} \simeq \Delta_{\text{true}} + \delta\Delta$ , where  $\Delta_{\text{true}} = \Delta(\omega, \mathbf{p}_{\text{true}})$  and  $\Delta_{\text{est}} = \Delta(\omega, \mathbf{p}_{\text{est}})$ . Systematic errors found in the parameter values produce systematic errors in the recovered total equivalent acceleration noise

$$\delta S_{n,f} \simeq \delta\Delta S_{n,o}\Delta^* + S_{n,o}\delta\Delta^*, \quad (42)$$

where the subscript “true” is dropped out for clearness. As pointed out in Ref. [34], the statistical uncertainty on the parameter values are masked by the statistical uncertainty on the estimated spectrum. Despite this, systematic errors in the estimated parameters can fall well outside the confidence levels of the optimal spectrum and show themselves as not mere excess noise, but producing really different noise shapes. Hence, it is expected that *the estimation of the total equivalent acceleration noise is biased*

*if the parameter values are not correctly assessed from system identification.*

To demonstrate the impact of system identification on the estimation of the total equivalent acceleration noise, a very long noise run,  $\sim 6$  days, is simulated with the same procedures of Sec. IV, i.e., by coloring a sequence of white Gaussian input time series with cross-correlating noise shaping filters. The interferometric displacement noise model is derived in a nonstandard configuration of LPF, as in Sec. VI G, namely, in the case of stronger-than-expected TM couplings, malfunctioning actuators, and a higher sensing cross-talk. In this case, the estimation of the total equivalent acceleration noise with naively guessed parameter values will surely contain systematic errors.

The estimation of the total equivalent acceleration noise is readily performed on the multichannel interferometric run with a scheme described in details in Refs. [18,34] by applying a time-domain version of the  $\Delta$  operator of Sec. III C. The issues connected to numerical derivatives in LPF are extensively discussed and solved in Ref. [35]. As said, system identification effectively helps in the calibration of the operator. In support of the statement, the numerical estimation of the total equivalent acceleration noise is performed assuming three different parameter sets which can be found in Table VIII:

- (1) the initial guess values, as it was *without* a preliminary system identification:  $\omega_1^2 = -1.3 \times 10^{-6} \text{ s}^{-2}$ ,  $\omega_{12}^2 = -0.7 \times 10^{-6} \text{ s}^{-2}$ ,  $S_{21} = 0$ ,  $A_{\text{df}} = 1$ ,  $A_{\text{sus}} = 1$  (typically  $\sim 10^4$  standard deviations away from the real values);
- (2) the best-fit values, as it was *with* a preliminary system identification, i.e., after having calibrated the differential operator:  $\omega_1^2 = -2.9998(2) \times 10^{-6} \text{ s}^{-2}$ ,  $\omega_{12}^2 = -2.0000(1) \times 10^{-6} \text{ s}^{-2}$ ,  $S_{21} = -1.4998(1) \times 10^{-3}$ ,  $A_{\text{df}} = 0.61994(8)$ ,  $A_{\text{sus}} = 0.599990(8)$ ;
- (3) the true values, used for consistency checks:  $\omega_1^2 = -3 \times 10^{-6} \text{ s}^{-2}$ ,  $\omega_{12}^2 = -2 \times 10^{-6} \text{ s}^{-2}$ ,  $S_{21} = -1.5 \times 10^{-3}$ ,  $A_{\text{df}} = 0.62$ ,  $A_{\text{sus}} = 0.6$ .

The result of the analysis is contained in Fig. 19, showing the total equivalent differential acceleration noise, both numerically estimated and modeled, for the three different cases.

First, the agreement between modeled and estimated total equivalent acceleration noise PSDs states that: (i) the generation of the interferometric noise is accurate to the assumed models at least to within the statistical uncertainty of the spectra; and (ii) the numerical estimation of the total equivalent acceleration in time domain is accurately explained by the frequency-domain transfer matrix from interferometric readouts to the total equivalent acceleration.

Second, but more important, the total equivalent acceleration noise estimated with a preliminary system

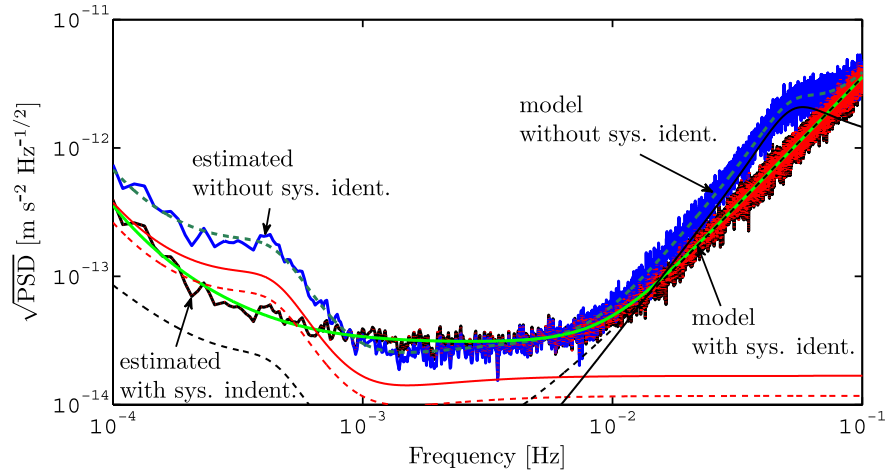


FIG. 19 (color online). Total equivalent differential acceleration noise numerically estimated on synthetic data and compared to theoretical noise models obtained by a full projection of fundamental noise sources. The estimation of the total out-of-loop equivalent acceleration can be performed either with a preliminary system identification or without it. The PSD estimated with a preliminary system identification completely overlaps the one of a hypothetical estimation assuming the knowledge of the true parameter values. The observed difference shows that a preliminary system identification is mandatory to avoid systematic errors in the reconstructed total equivalent acceleration noise. The solid thinner lines indicate the reasons of such a discrepancy. Around 50 mHz, the bump is due to unsuppressed thruster noise exceeding the interferometric  $\sigma_{12}$  readout noise. At low frequency and around 0.4 mHz, the two major contributions are the unsuppressed force couplings between the TMs and the SC and the capacitive actuation noise. Thanks to system identification, an improvement in performance of a factor 4 at low frequency is evident.

identification completely overlaps the one of a hypothetical estimation assuming the complete knowledge of the true values. Therefore, it demonstrates that it is still possible to meet the sensitivity requirements during underperforming mission operations.

The observed systematic errors in the total equivalent acceleration noise estimated without identification show that system identification is strictly mandatory to avoid such problems and guarantees the scientific objectives. The systematic errors can be explained by the fact that the naive initial guess values are sensitively different from the true values. Since the operator is not calibrated on fiducial parameter values, it is not effective in compensating, in turn, the SC jitter due to the thruster actuation noise, the TM couplings, and the capacitive actuation noise. In particular, around 50 mHz, the bump is the unsuppressed thruster noise exceeding the interferometric  $\sigma_{12}$  readout noise: the effect is due to the uncalibrated drag-free gain  $A_{df}$ . At low frequency and around 0.4 mHz, the major contributions are the coupling forces between the TMs and the SC (two contributions, accounting for  $1.8 \times 10^{-13} \text{ m s}^{-2}$ , almost the whole noise budget) and the capacitive actuation noise ( $7 \times 10^{-14} \text{ m s}^{-2}$ ); the effect is due to the uncalibrated stiffness constants  $\omega_1^2$  and  $\omega_{12}^2$  and the suspension gain  $A_{sus}$ .

The final improvement in the estimated total equivalent acceleration noise with system identification is a factor 4 around 0.4 mHz and a factor 2 around 50 mHz in units of  $\sqrt{\text{PSD}}$ . The conclusion is that without a preliminary system identification—robust to nonstandard parameter values—the performance of the mission and the characterization of

the total equivalent acceleration noise would seriously be compromised.

## VIII. CONCLUDING REMARKS

This work focused on the maximum likelihood estimation in time domain of the key parameters modeling the dynamics of TMs in the LPF mission. After introducing the dynamical equations and a model for LPF, with its physical parameters and their significance, we showed how to handle the effect of the controller, measure all known forces, including the control forces, and subtract them from the data in order to provide an estimate of the residual acceleration noise acting between the TMs—the scientific objective of LPF.

We discussed our multiexperiment/multichannel approach as a method to reach the desired measurement accuracy. We started the discussion with a Monte Carlo simulation of different noise realizations, showing the statistical consistency of the method at the level of parameter statistics, variance statistics, and log-likelihood statistics, all remarkably in accordance with the theoretical expectations.

Considering the realistic possibility that our knowledge of the system is not sufficient or the system is highly underperforming, we tested the robustness against a couple of nonstandard scenarios. In the first example, we explored the situation in which the optical readouts are affected by a non-negligible amount of non-Gaussianities: the manifestation of glitches as failures in the electronic devices. The result was that we are still able to estimate unbiased values

of the system parameters by identifying those most sensitive to non-Gaussianities. We also proposed a method to handle data corrupted by outliers in parameter estimation, consisting of a step-by-step reweighing process. In the second example, we examined a very unfortunate situation in which the forces, coupling the TMs to the SC, are stronger than expected, and the actuators (both the thrusters and the capacitive suspensions) malfunction properly due to hardware failures. Again, the result was that we are able to estimate unbiased values of the system parameters and recover the instrumental noise shapes with an evident improvement in the fit residuals.

The same methodology was employed to analyze data produced by a realistic LPF simulator in use at ESA during operational exercises. The scope is to enter into a mission-like routine, operating a system where many parameters are unknown.

Finally, since the final goal of the LPF mission is the characterization of the LISA arm in terms of differential acceleration, we proved for the first time that the proposed parameter estimation—and, in general, system identification—is mandatory for the correct assessment of the differential residual acceleration noise. Otherwise, systematic errors may arise in the reconstructed acceleration noise, having a profound impact on the GW astronomy in the low-end LISA band.

## APPENDIX A: DEMONSTRATION OF NOISE NONSTATIONARITY

We demonstrate the validity of Eq. (20), i.e., that the fluctuation of any of the system parameter produces non-stationary noise. Expanding the noise around some nominal parameter value  $p_0$ , up to first order and computing the variance of the interferometric noise, it reads

$$\begin{aligned} \text{Var}[o] &\simeq \text{Var}[o_0] + \text{Var}[o' \delta p] + 2\text{Cov}[o_0, o' \delta p] \\ &= \text{Var}[o_0] + \text{Var}[o'] \delta p^2 + 2\text{Cov}[o_0, o'] \delta p, \end{aligned} \quad (\text{A1})$$

where  $\text{Var}[o']$  and  $\text{Cov}[o_0, o']$  are the variance of the noise first derivative and the covariance between the zeroth order and the first derivative. So, for a zero-mean process with finite second moment, it holds

TABLE IX. Sample mean  $\mu$ , standard deviation  $\sigma$  and higher moments, the sample skewness  $\gamma_1$  and the excess kurtosis  $\gamma_2$ , for the whitened data channels  $o_1$  and  $o_{12}$ . Assuming Gaussian-distributed data, the approximate standard deviations are  $\sigma_\mu \simeq \sigma/\sqrt{N}$ ,  $\sigma_\sigma \simeq \sigma/\sqrt{2N}$ ,  $\sigma_{\gamma_1} \simeq \sqrt{6/N}$ ,  $\sigma_{\gamma_2} \simeq \sqrt{24/N}$ , with  $N$  the number of data samples.

Data	$\mu$	$\sigma$	$\gamma_1$	$\gamma_2$
$o_{1,w}$	$0.008 \pm 0.003$	$0.970 \pm 0.002$	$(-5 \pm 8) \times 10^{-3}$	$(0 \pm 2) \times 10^{-2}$
$o_{12,w}$	$-0.254 \pm 0.003$	$1.002 \pm 0.002$	$(0 \pm 8) \times 10^{-3}$	$(3 \pm 2) \times 10^{-2}$

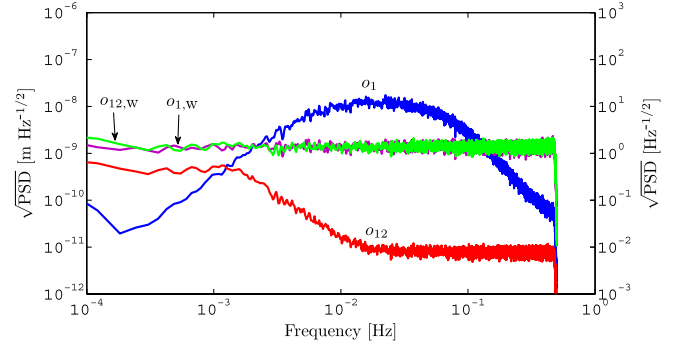


FIG. 20 (color online). Whitening of a simulated noise run.  $o_1$  and  $o_{12}$  are the two interferometer readings with PSD reported on the basis of the scale on the left-hand side.  $o_{1,w}$  and  $o_{12,w}$  are the whitened counterparts with PSD reported on the basis of the scale at the right-hand side. They show how the whitening filters can flatten the noise shapes. The convolution with a low-pass filter of the data resampling from 10 to 1 Hz is the cause of the drop around 0.5 Hz.

$$\begin{aligned} \text{Cov}[o_0, o'] &= E[o_0 o'] - E[o_0]E[o'] = E\left[\frac{1}{2} \frac{\partial}{\partial p} n^2\right] \\ &= \frac{1}{2} \frac{\partial}{\partial p} \text{Var}[n]. \end{aligned} \quad (\text{A2})$$

Substituting this result back into Eq. (A1), Eq. (20) is finally demonstrated.

## APPENDIX B: WHITENING

The colored noise behavior of a typical LPF run makes it mandatory to decorrelate the data used for system identification in order for a generic statistical estimator to be unbiased. Consider, for example, a stationary noisy time series  $o(t)$  with noise PSD  $S_n(\omega)$ . The SNR of the signal [28] can be recast as

$$\rho^2 = \int \frac{o^*(\omega)o(\omega)}{S_n(\omega)} d\omega = \int o_w^*(\omega)o_w(\omega) d\omega, \quad (\text{B1})$$

which can be viewed as the acting of the *whitening filter*  $W(\omega) = 1/\sqrt{S_n(\omega)}$  on  $o(\omega)$  to produce the whitened series

$$o_w(\omega) = W(\omega)o(\omega). \quad (\text{B2})$$

Here “whitened” is equivalent to saying that the noise PSD of the filtered series is approximately frequency-independent. The discrete time-domain version of the preceding involves the noise covariance matrix  $C_n$

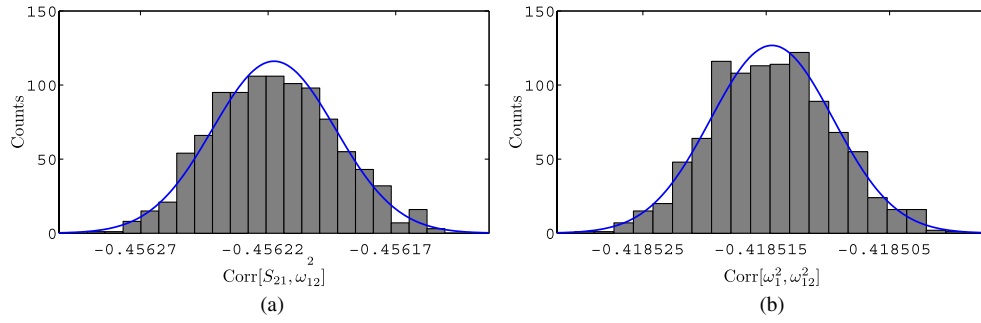


FIG. 21 (color online). Monte Carlo validation of 1000 independent noise realizations on which parameter estimation is repeated identically at each step. The statistics is shown for two parameter correlations. The scaled Gaussian PDF is evaluated at the sample mean and standard deviation.

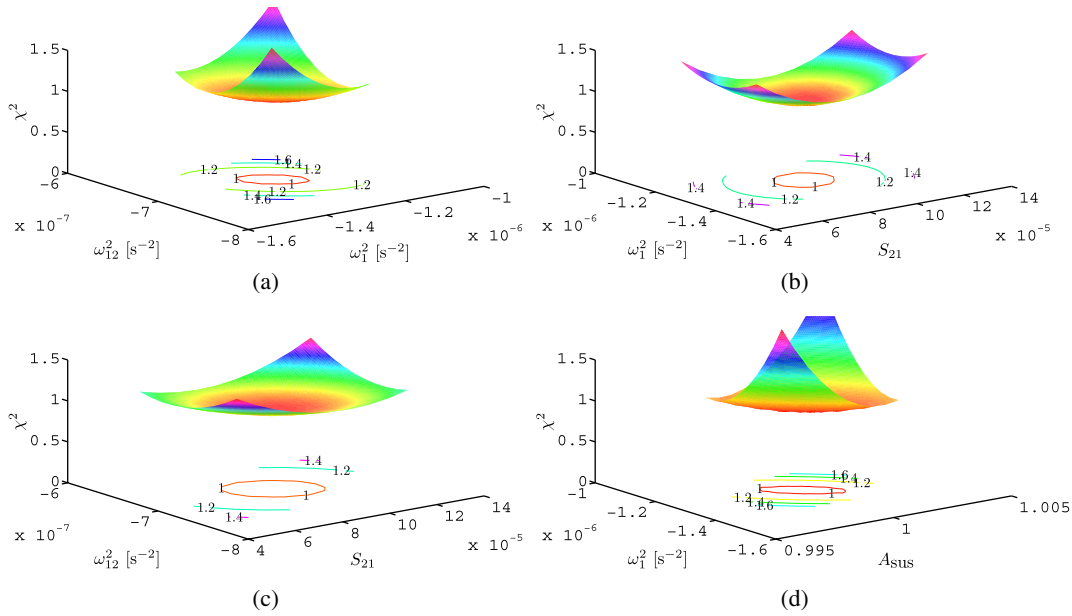


FIG. 22 (color online).  $\chi^2$  log-likelihood curvature around the best-fit values. The 7-dimensional surface are projected onto two parameters at a time for some examples. Correlation is the reason why the surface can be rotated.

$$\rho^2 = \mathbf{o}^T \mathbf{C}_n^{-1} \mathbf{o} = \mathbf{o}_W^T \mathbf{\Lambda}_n^{-1} \mathbf{o}_W, \quad (\text{B3})$$

which again can be viewed as the acting of the whitening filter  $\mathbf{W}$ , an orthogonal matrix satisfying  $\mathbf{C}_n^{-1} = \mathbf{W}^T \mathbf{\Lambda}_n^{-1} \mathbf{W}$  [36], on  $\mathbf{o}$  to produce the whitened unit-variance series

$$\mathbf{o}_W = \mathbf{W}\mathbf{o}. \quad (\text{B4})$$

As above, whitened means that the process diagonalizes the covariance matrix, so that  $\mathbf{\Lambda}_n$  effectively becomes an identity matrix.

For simulation and analysis purposes, whitening a time series is formally the inverse process of noise generation. Whitening filters are obtained by performing a fit in the  $z$  domain to the inverse of the estimated PSD. Figure 20 reports an example of whitening [37] a typical 28-hour run of interferometric noise. The effect of the whitening filters,

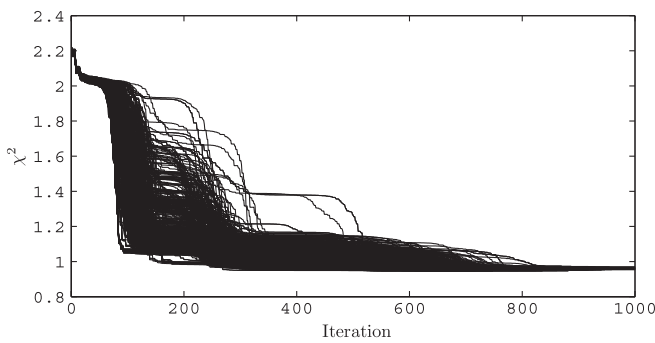


FIG. 23. Monte Carlo fit  $\chi^2$  chains. The processes typically last for  $\sim 1000$  iterations and stop when either the function or the variable tolerance is below  $1 \times 10^{-4}$ .

as required, is to flatten the noise shapes, i.e., to decorrelate the time series.

Despite the PSD shapes which seem reasonably good at first sight, a residual red component still persists. Table IX reports two higher-order moments (skewness and excess kurtosis) of the empirical distribution together with their uncertainties [27]. By inspecting the values, it turns out that the sample mean of the differential channel  $o_{12}$  is not compatible with zero, as one would expect. Usually, a first- or second-order polynomial fit is necessary to subtract that residual component. The result is not surprising: the intrinsic difficulty is that the whitening process is performed on a restricted frequency band (the one of the estimated PSD), and low-frequency components may survive after the filtering.

### APPENDIX C: MORE ON MONTE CARLO VALIDATION

This section investigates a little further on the Monte Carlo simulation of Sec. VIE, which demonstrated that all parameters are unbiased and Gaussian-distributed, as well as their variances.

Surprisingly, the correlations are also Gaussian-distributed with good approximation. See Fig. 21 for two examples.

The correlation between two parameters is somehow related to the rotation of the  $\chi^2$  paraboloid principal axes around the minimum. To support this statement, Fig. 22 shows few examples of projections of the 7-dimensional surface onto two parameters at a time, around the best-fit values. Weakly correlated parameters, like  $S_{21}$  and  $\omega_1^2$  ( $\sim 20\%$ ) [panel (b)], typically have the principal axes of the contour curves aligned with the  $x$  and  $y$  axis. Highly correlated parameters, like  $A_{\text{sus}}$  and  $\omega_1^2$  ( $\sim -70\%$ ) [panel (d)], have the principal axes which are significantly rotated.

Figure 23 shows a record history of all Monte Carlo estimation chains. The scatter of the chains is due to the noise fluctuation along the Monte Carlo iterations. There are clearly some chains which are far away from the accumulation zone; this behavior is quite unexpected as one would think the noise would have little impact on the chain locations. Despite the big scatter, the asymptotic distribution is Gaussian, as elucidated in Fig. 14.

- 
- [1] P. Bender *et al.*, Study Report No. MPQ 233, 1998.
- [2] K. Danzmann *et al.*, Assessment Study Report No. ESA/SRE 3, 2011.
- [3] S. Vitale, *Space Sci. Rev.* **148**, 441 (2009).
- [4] S. Vitale *et al.*, *Nucl. Phys. B, Proc. Suppl.* **110**, 209 (2002).
- [5] F. Antonucci *et al.*, *Classical Quantum Gravity* **28**, 094001 (2011).
- [6] P. Amaro-Seoane, J.R. Gair, M. Freitag, M. Coleman Miller, I. Mandel, C.J. Cutler, and S. Babak, *Classical Quantum Gravity* **24**, R113 (2007).
- [7] F. Antonucci *et al.*, *Classical Quantum Gravity* **28**, 094002 (2011).
- [8] G. Congedo, F. De Marchi, L. Ferraioli, M. Hueller, S. Vitale, M. Hewitson, N. Nofrarias, A. Monsky, M. Armano, A. Grynagier, M. Diaz-Aguilo, E. Plagnol, and B. Rais, JPCS Proc. of the 8th International LISA Symposium, Stanford University, 2011 (unpublished), [arXiv:1108.0865](https://arxiv.org/abs/1108.0865).
- [9] LTPDA Toolbox, <http://www.lisa.aei-hannover.de/ltpda>.
- [10] MATLAB, <http://www.mathworks.com>.
- [11] F. Steier, F. Guzmán Cervantes, A.F. García Marin, D. Gerardi, G. Heinzel, and K. Danzmann, *Classical Quantum Gravity* **26**, 094010 (2009).
- [12] W. Fichter, P. Garth, S. Vitale, and D. Bortoluzzi, *Classical Quantum Gravity* **22**, S139 (2005).
- [13] A. Grynagier, W. Fichter, and S. Vitale, *Classical Quantum Gravity* **26**, 094007 (2009).
- [14] ASTRIUM-EADS, <http://www.astrium.eads.net>.
- [15] F. Antonucci *et al.*, *Classical Quantum Gravity* **28**, 094006 (2011).
- [16] M. Armano *et al.*, *Classical Quantum Gravity* **26**, 094001 (2009).
- [17] G. Congedo, Ph.D. thesis, University of Trento, Italy, 2012, [arXiv:1204.4299](https://arxiv.org/abs/1204.4299).
- [18] A. Monsky *et al.*, *Classical Quantum Gravity* **26**, 094004 (2009).
- [19] G. Hechenblaikner, R. Gerndt, U. Johann, P. Luetzow-Wentzky, V. Wand, H. Audley, K. Danzmann, A. Garcia-Marin, G. Heinzel, M. Nofrarias, and F. Steier, *Appl. Opt.* **49**, 5665 (2010).
- [20] M. Nofrarias, C. Röver, M. Hewitson, A. Monsky, G. Heinzel, and K. Danzmann, *Phys. Rev. D* **82**, 122002 (2010).
- [21] Following Eq. (10), a bias in the guidance signals is equivalent to a commanded force bias directly applied onto the SC through thruster actuation and the second TM through capacitive actuation.
- [22] L. Ferraioli, Mauro Hueller, and Stefano Vitale, *Phys. Rev. D* **82**, 042001 (2010).
- [23] Throughout this paper, if not otherwise stated, it is assumed that a PSD is estimated by means of the Welch (modified periodogram) method [24] using a 4-sample 92 dB Blackman-Harris window [25], 16-segments averaged, 66% overlap, and mean detrended.
- [24] P. Welch, *IEEE Trans. Audio Electroacoust.* **AU-15**, 70 (1967).
- [25] F. Harris, *Proc. IEEE* **66**, 51 (1978).
- [26] The numerical implementation of the direct and inverse Fourier transform are the fast Fourier transform (FFT) and inverse FFT (IFFT). Being circular operations, the input time series needs to be zero-padded to avoid systematic

- errors caused by wrapped-around data [27]. A conservative default value of one data length is assumed.
- [27] W. H. Press, S. A. Teukolsky, W. T. Vetterling, and B. P. Flannery, *Numerical Recipes* (Cambridge University Press, Cambridge, England, 2007).
- [28] L. Finn, *Phys. Rev. D* **46**, 5236 (1992).
- [29] M. Vallisneri, *Phys. Rev. D* **77**, 042001 (2008).
- [30] M. Vallisneri, *Phys. Rev. Lett.* **107**, 191104 (2011).
- [31] SIMULINK, <http://www.mathworks.com>.
- [32] M. Nofrarias, L. Ferraioli, G. Congedo, M. Heuller, M. Armano, M. Diaz-Aguilo, A. Grynagier, M. Hewitson, and S. Vitale, Proc. of the 9th Edoardo Amaldi Conference on Gravitational Waves, Cardiff University, 2011 (unpublished), [arXiv:1111.4916](https://arxiv.org/abs/1111.4916).
- [33] L. Ferraioli, Giuseppe Congedo, Mauro Hueller, and Stefano Vitale, *Phys. Rev. D* **84**, 122003 (2011).
- [34] L. Ferraioli, M. Armano, G. Congedo, M. Diaz-Aguilo, F. De Marchi, A. Grynagier, M. Hewitson, M. Heuller, A. Monsky, M. Nofrarias, E. Plagnol, B. Rais, and S. Vitale, Proc. of the 8th International LISA Symposium, Stanford University, 2011 (unpublished), [arXiv:1111.4816](https://arxiv.org/abs/1111.4816).
- [35] L. Ferraioli, M. Heuller, and S. Vitale, *Classical Quantum Gravity* **26**, 094013 (2009).
- [36] In fact, if  $C_n = U^T \Lambda_n U$  where  $U$  is an orthogonal matrix and  $\Lambda_n$  is the eigen-decomposition of  $C_n$ , then it turns out that  $U^{-1} = W^T$ .
- [37] Data filtering can produce fake transients at the beginning of the filtered time series. To avoid this possibility, an initial segment of data is usually cut away.